Chemical Geology 420 (2016) 186–199

Contents lists available at ScienceDirect

Chemical Geology

journal homepage: www.elsevier.com/locate/chemgeo

Chemical and O-isotope compositions of amphiboles and clinopyroxenes from A-type granites of the Papanduva Pluton, South Brazil: Insights into late- to post-magmatic evolution of peralkaline systems

Frederico C.J. Vilalva [a,*], Silvio R.F. Vlach [b], Antonio Simonetti [c]

[a] Departamento de Geologia, Centro de Ciências Exatas e da Terra, Universidade Federal do Rio Grande do Norte, Campus Universitário Lagoa Nova, Natal, RN 59078-970, Caixa Postal 1639, Brazil
[b] Departamento de Mineralogia e Geotectônica, Instituto de Geociências, Universidade de São Paulo, Rua do Lago, 562, Cidade Universitária, São Paulo, SP 05508-080, Brazil
[c] Department of Civil and Environmental Engineering and Earth Sciences, University of Notre Dame, Notre Dame, IN 46556, USA

ARTICLE INFO

Article history:
Received 18 May 2015
Received in revised form 13 November 2015
Accepted 17 November 2015
Available online 18 November 2015

Keywords:
Amphibole
Clinopyroxene
Trace elements
Oxygen isotope ratio
Late- to post-magmatic evolution
Peralkaline granites

ABSTRACT

Clinopyroxene and amphibole are the main mafic minerals in peralkaline granites of the Papanduva Pluton, Morro Redondo Complex, one of the most important granitic occurrences within the Graciosa A-type Province, S-SE Brazil. Clinopyroxene is present as three distinct late- to post-magmatic textural generations of aegirine, as well as post-magmatic aegirine–augite. Amphibole is predominantly magmatic ferrorichterite and arfvedsonite, and post-magmatic riebeckite. Major and trace element compositions reveal evolutionary trends characterized by increasing Fe^{3+} and Na and decreasing Fe^{2+}, Ca, HFSE, and REE contents from core to crystal rims; trace element and REE partitioning is controlled by the composition of the coexisting melts or fluid phases, as well as by crystal chemistry. $\delta^{18}O$ values for minerals investigated range from +2.3 to +6.4‰ and correlate both with increasing degrees of alkalinity and quasi-solidus (sub-magmatic) deformation affecting several granites of the Papanduva Pluton. These deformation events played a significant role in the concentration and circulation of residual melts and fluid phases from which amphiboles and clinopyroxenes precipitated. Combined textural, chemical, and O isotope findings suggest that these fluids evolved through more oxidizing (close to the FMQ buffer), alkali- (i.e. peralkaline), fluorine-, and ^{18}O-rich conditions, associated with higher abundances of HFSEs and REEs within a temperature interval between 750 and 700 °C (late-magmatic stages) and 400–450 °C (post-magmatic stages).

1. Introduction

Alkaline felsic rocks are marked by the ubiquity of clinopyroxene and/or amphibole, which typically form during primary, late, and hydrothermal stages of magmatic evolution for a given pluton. In particular, the crystallization of aegirine and arfvedsonite as opposed to fayalite or magnetite is a typical feature of the transition from metaluminous to peralkaline melt compositions (e.g. Markl et al., 2010; Marks et al., 2003). The petrogenetic importance of both clinopyroxene and amphibole is justified by their extensive chemical variability and the potential to incorporate a large number of geochemically relevant trace elements (Wood and Blundy, 1997; Marks et al., 2004). Such characteristics render these minerals as powerful tools to unravel the chemical evolution of magmatic and late- to post-magmatic liquids, and post-magmatic fluids from which they have crystallized (e.g., Giret et al., 1980; Strong and Taylor, 1984; Salviulo et al., 2000; Marks et al., 2004; Gualda and Vlach, 2007b; Schilling et al., 2011; Reguir et al., 2012). Of importance, clinopyroxene can be a sensitive indicator of fractionation processes (e.g., Neumann, 1976; Marks et al., 2004; Piilonen et al., 2013), while compositional variations in amphibole may reflect the alumina saturation index and, consequently, the degree of magma alkalinity, as well as the redox conditions during crystallization (e.g., Giret et al., 1980; Strong and Taylor, 1984; Papoutsa and Pe-Piper, 2014).

Sodic–calcic and sodic clinopyroxene and amphibole are the main ferromagnesian minerals in peralkaline granites of the Papanduva Pluton, Morro Redondo Complex, Graciosa Province (southernmost Brazil). These granites are of particular interest in relation to mineralogical studies of oversaturated peralkaline systems, as they include the most evolved peralkaline rocks within the province and several host a variety of rare Zr-, Ti-, Nb-, and REE-rich accessory minerals (e.g., Vilalva et al., 2013).

This work reports textural studies, chemical (major, minor and trace elements), and oxygen isotope data for Na–Ca- and Na-clinopyroxene and amphibole of distinct textural generations in the Papanduva Pluton. The integrated results are used to provide inferences on late- to post-magmatic evolution trends, crystallization conditions, reaction relationships among these phases, and the possible role of sub-magmatic deformation in controlling liquid composition and fluid circulation.

* Corresponding author.
E-mail addresses: fredcjv@ufrnet.br (F.C.J. Vilalva), srfvlach@usp.br (S.R.F. Vlach), simonetti.3@nd.edu (A. Simonetti).

http://dx.doi.org/10.1016/j.chemgeo.2015.11.019
0009-2541/

2. Geological background

The Morro Redondo Complex (Fig. 1) includes the Papanduva Pluton (~60 km^2), made up of peralkaline alkali-feldspar granites, and the larger Quiriri Pluton, which consists of subalkalic biotite (± hornblende) syenogranites, and associated volcanics. The complex belongs to the Neoproterozoic (580–583 Ma) A-type Graciosa Province emplaced during a post-collisional, extensional, tectonic regime in southern Brazil (Gualda and Vlach, 2007a; Vlach et al., 2011).

The Papanduva Pluton is composed of leucocratic (M′ = 2–9) alkali-feldspar granites with variable quartz contents and low magnetic susceptibilities (<1.0×10^{-3} SI) that are grouped into four petrographic facies (cf. Fig. 1) as follows (see also Vilalva and Vlach, 2014):

1. *Massive facies*: the main facies, with slightly inequigranular, medium- to coarse-grained texture, containing sodic–calcic and sodic amphibole and clinopyroxene as the main mafic minerals, and zircon, astrophyllite, aenigmatite, fluorite, titanite, and chevkinite as accessories;
2. *Deformed facies*: of localized occurrence, it is characterized by a general *cataclastic* aspect, as evidenced by slightly deformed quartz and alkali-feldspar megacrysts and moats of recrystallized quartz. Sodic clinopyroxene is the main mafic mineral, along with some sodic amphibole. Accessory minerals include zircon, astrophyllite, aenigmatite, ilmenite, and chevkinite; allanite and magnetite are typical post-magmatic phases;
3. *Foliated facies*: characterized by deformational structures with variable degrees of intensity that imprints porphyroclastic and protomylonitic textures. Ellipsoidal to irregularly shaped sodic amphibole, alkali-feldspar and quartz megacrysts occur in a saccharoidal quartz–feldspathic matrix that hosts several rare Ti-, Nb- and REE-bearing late- to post-magmatic accessory minerals, such as aenigmatite, neptunite, narsarsukite, britholite-(Ce), nacareniobsite-(Ce), (Na,K)-zirconosilicates, and turkestanite; zircon is absent (cf. Vilalva et al., 2013);
4. *Micrograniticfacies*: slightly inequigranular, fine-grained dike rocks that intrude units within the massive facies, as well as the biotite syenogranites from the Quiriri Pluton. Typical accessories are zircon and (Zn,Mn)-rich ilmenite. Magnetite is a typical post-magmatic phase.

Micro-structures and textures of facies 2 and 3 indicate submagmatic deformation conditions (cf. Blenkinsop, 2000), with melt-present rather than pure solid-state crystal deformation. Their main difference is related predominantly to the degree of deformation.

These granites are characterized by an agpaitic-like crystallization sequence, in which the mafic minerals and most accessories precipitated after the felsic phases, filling in the remaining interstices. Geochemical features are akin to those described for peralkaline granites elsewhere (e.g., Bonin, 2007; Frost and Frost, 2011). They include high alkali contents (8.7 < $Na_2O + K_2O$ wt.% < 9.3) and fe# numbers [FeO^T / (FeO^T + MgO), wt.%] ≥ 0.96; the Agpaitic [AI = ($Na_2O + K_2O$) / Al_2O_3 mol] and Alumina Saturation [ASI = Al_2O_3 / ($CaO + Na_2O + K_2O$) mol] Indices vary between 1.04–1.28, and 0.76–0.94, respectively. High-field strength elements (HFSEs), especially Zr, Nb, Y, and REEs abundances are relatively high (up to 2430, 88, 320, 996 ppm, respectively) and positively correlated with AI contents.

3. Analytical methods and data treatment

A detailed textural and chemical study was conducted of distinct textural generations of amphibole and clinopyroxene from the petrographic facies of the Papanduva Pluton. Major and minor elements were quantified by electron-probe microanalyses (EPMA) and trace element abundances were measured by laser ablation inductively coupled plasma mass spectrometry (LA-ICP-MS) analyses. Oxygen isotope determinations were obtained in selected mineral concentrates using a laser fluorination system coupled to a silicate extraction line and isotope ratio mass spectrometer.

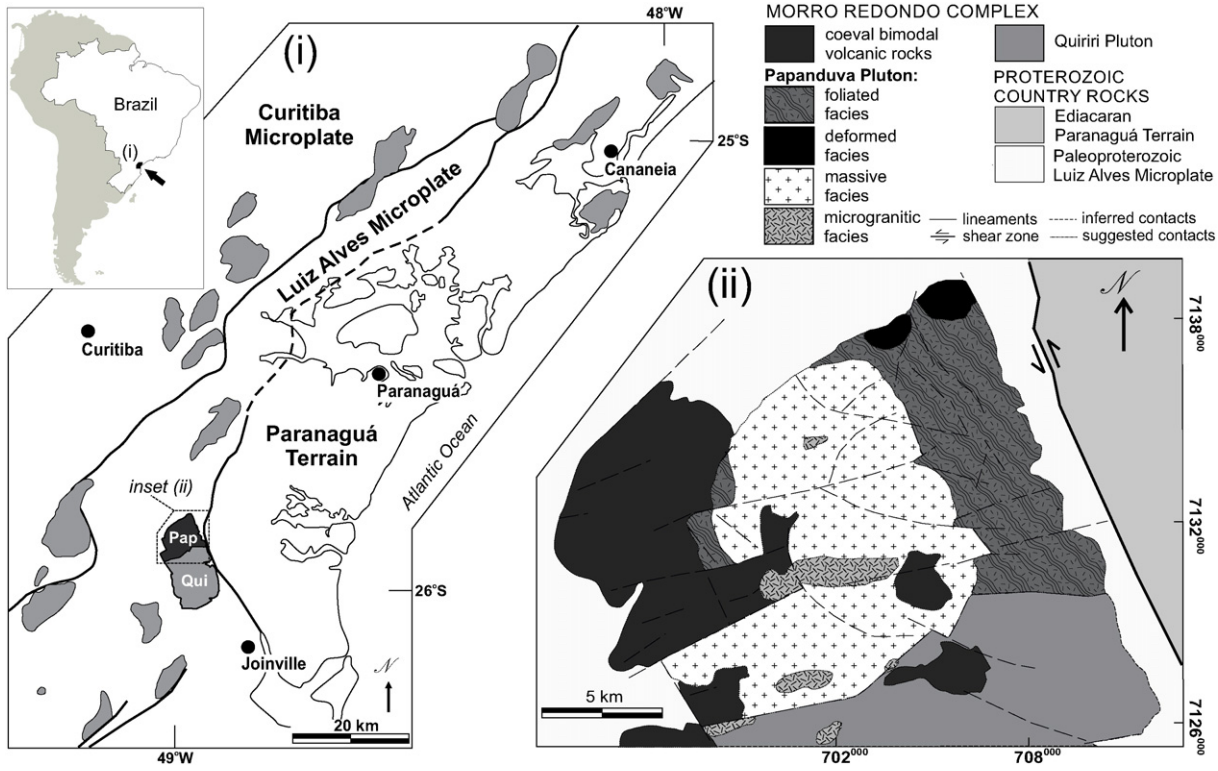

Fig. 1. Geological location and setting of the Morro Redondo Complex. (i) The Neoproterozoic A-type Graciosa Province in S-SE Brazil illustrating the location of the Morro Redondo Complex, where Pap = Papanduva Pluton and Qui = Quiriri Pluton. (ii) Detailed geological map of the Papanduva Pluton within the Morro Redondo Complex.

A full description of the analytical procedures and data treatment is given in Appendix A.

4. Main textural features

4.1. Amphiboles

Sodic and sodic–calcic amphiboles are the most abundant mafic minerals in the Papanduva Pluton rocks. Sodic amphiboles include arfvedsonite and riebeckite, the latter restricted to the deformed and microgranitic facies. They crystallized as isolated or aggregates of 3–5 subhedral to anhedral (interstitial) crystals (1 to 5 mm long). Arfvedsonite is typically magmatic (Fig. 2A to C); most crystals show dark colored cores, with irregular outlines suggesting late re-equilibration episodes (e.g., Schilling et al., 2011), and surrounded by light colored rims. Riebeckite is a late phase; its association with alkali-feldspar exsolution textures and with hydrothermal magnetite and zircon growth on early amphibole and pyroxene (Fig. 2D) suggest a post-magmatic crystallization. A distinct late-crystallizing variety of arfvedsonite is found in granites of the massive facies as minute pristine, light blue, euhedral crystals. In the foliated facies, arfvedsonite appears as fractured, elongated or rounded megacrysts (Fig. 2A and K).

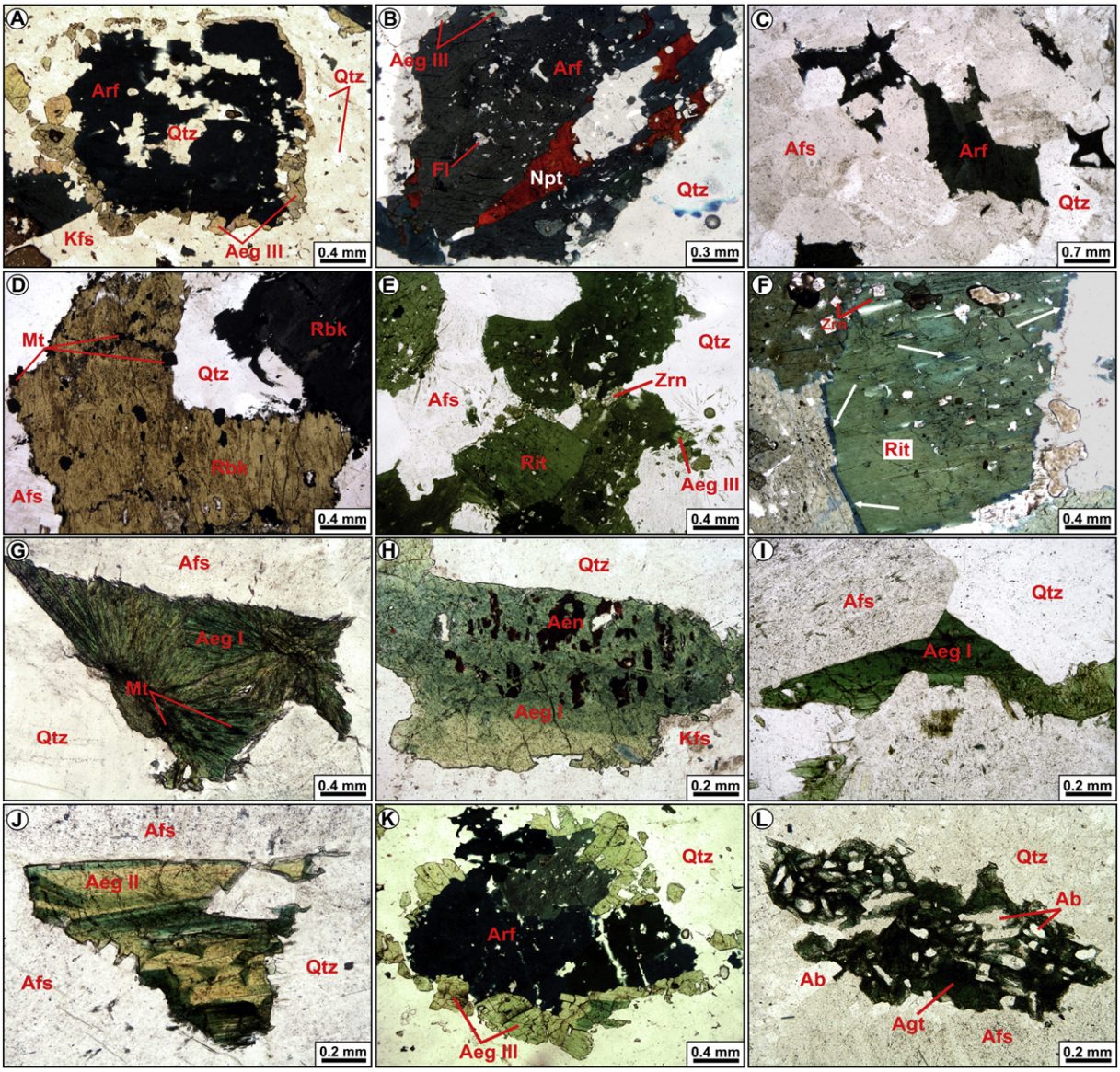

Fig. 2. Microscopic aspects of amphibole (A to F) and clinopyroxene (G to L) from the Papanduva Pluton. All photomicrographs obtained under plane polarized light. (A) Arfvedsonite megacryst in a matrix of quartz and potassic feldspar mantled by aegirine III crystals in foliated alkali feldspar granite. (B) Arfvedsonite megacryst among quartz crystals in foliated alkali feldspar granite. Neptunite and aegirine III replace the amphibole along fracture planes and rims; note inclusions of fluorite and quartz in the core region. (C) Arfvedsonite crystals interstitial to quartz and alkali feldspar in alkali feldspar microgranite. (D) Riebeckite megacryst with post-magmatic magnetite crystals along cleavage and fracture planes, and close to rim zones in deformed alkali feldspar granite. (E) Ferrorichterite crystals interstitial to quartz and alkali-feldspar in massive alkali feldspar granite; note small quartz and zircon inclusions and replacement by aegirine III. (F) Detail of late arfvedsonite overgrowth (white arrows) over ferrorichterite crystal in massive alkali feldspar granite; note quartz and zircon inclusions. (G) Fibrous aggregate of aegirine I crystals partially replaced by magnetite in deformed alkali feldspar granite (H) Crystal of aegirine I with anhedral relics of aenigmatite in foliated alkali feldspar granite. The green-colored core with aenigmatite relics are Ca-, Ti- and Fe^{2+}-rich. (I) Late-magmatic aegirine I crystal interstitial to quartz and alkali feldspar crystals in massive alkali feldspar granite; dark-green crystal zones are Ca-, Ti- and Fe^{2+}-rich. (J) Aegirine II crystal with the typical greenish-orange pleochroic scheme interstitial to quartz and alkali feldspar in massive alkali feldspar granite. (K) Crystals of post-magmatic aegirine III replacing arfvedsonite megacryst in a quartz-rich matrix of foliated alkali feldspar granite; note quartz also as inclusions in arfvedsonite. (L) Interstitial aegirine–augite with poikilitic-like texture encompassing laths and anhedral crystals of albite, among alkali feldspar, quartz and albite crystals in a massive alkali feldspar granite. Mineral abbreviations: Ab = albite; Aeg = aegirine (I, II, and III are different textural generations); Aen = aenigmatite; Afs = alkali feldspar; Agt = aegirine–augite; Arf = arfvedsonite; Fl = fluorite; Kfs = potassic feldspar; Mt = magnetite; Npt = neptunite; Qtz = quartz; Rbk = riebeckite; Rit = ferrorichterite; Zrn = zircon.

The sodic–calcic amphibole corresponds to ferrorichterite, which is a predominant, earlier-formed phase restricted to the granites from the massive facies. It appears as aggregates of 2–3 subhedral crystals (2.0–6.0 mm long) with subtle compositional zoning (Fig. 2E) and late overgrowths of arfvedsonite (Fig. 2F).

Late- to post-magmatic and hydrothermal amphibole substitution reactions lead to the crystallization of a variety of minerals along its rims, fractures, and cleavage planes. These include aegirine mantles (Fig. 2A and K), neptunite (Fig. 2B), astrophyllite, and magnetite; the latter being particularly common in the deformed (Fig. 2D) and microgranitic facies.

4.2. Clinopyroxene

Clinopyroxene is a ubiquitous phase in all granites and the main mafic mineral in the deformed facies and in some microgranites. Four distinct textural generations are recognized: *aegirine I* — late-magmatic crystals; *aegirine II* — late- to post-magmatic crystals; *aegirine III* — late- to post-magmatic crystals, typically as mantles over amphiboles, and *aegirine–augite* as post-magmatic.

Aegirine I has a subtle greenish pleochroism and is the dominant variety in all granites. Zoning patterns are irregular, patchy, hourglass, or concentric; the latter contain dark cores surrounded by light colored rims (Fig. 2H). It occurs as isolated interstitial grains (Fig. 2I), or in aggregates of subhedral to euhedral (fibrous in the cataclastic facies; Fig. 2G) crystals. Textural relationships, as shown in Fig. 2H, indicate that some crystals replace previously formed aenigmatite. Aegirine I is replaced by narsarsukite during late- to post-magmatic stages in the foliated facies, and by magnetite in the post-magmatic stage of the deformed facies (Fig. 2G). Laths of albite and minute fluorite are typical inclusions.

Aegirine II, with a greenish-orange pleochroic scheme, occurs as sparse grains. Orange cores and greenish rims define a discrete concentric zoning (Fig. 2J). Textural evidences suggest it crystallized after aegirine I. Aegirine II is absent in microgranites.

Aegirine III is a distinct late- to post-magmatic generation that replaces amphiboles along fractures, cleavages, and around their rims, forming continuous or discontinuous mantles (Fig. 2A, E and K). Laths of almost pure albite, as well as minute quartz and fluorite are common inclusions.

Aegirine–augite is a relatively rare mineral in the foliated and massive facies. It forms homogeneous dark green-colored crystals, sometimes in poikilitic-like arrangement with quartz and albite laths (Fig. 2L).

5. Major element compositional variations

The complete EPMA data set and structural formulae for amphibole and clinopyroxene are available as supplementary material. Their main compositional characteristics are presented and discussed below.

5.1. Amphibole

The Papanduva amphiboles are characterized by low mg# [= $Mg/(Mg + Fe^{2+})$] numbers (<0.01 to 0.06). Ferrorichterite in the massive facies is a Ca-rich variety, with relatively high Ti (up to 0.3 atoms per formula unit, apfu, or 2.4 wt.% TiO_2) and Mg (up to 0.2 apfu or 0.8 wt.% MgO) contents. The main arfvedsonite in this facies has Ti up to 0.25 apfu (2.1 wt.% TiO_2) and Ca up to 0.39 apfu (2.3 wt.% CaO), with partially filled [A] sites ($Na^A + K^A < 1.0$), while the late-stage minute pristine crystals and overgrowths around ferrorichterite contain lower Ti (0.02 apfu or 0.2 wt.% TiO_2), and Ca (up to 0.17 apfu or 1.0 wt.% CaO) contains.

Arfvedsonite found in the foliated facies records the highest alkali contents (up to 2.8 apfu Na or 9.0 wt.% Na_2O, and 0.83 apfu K or 4.1 wt.% K_2O) and the strongest compositional zoning. Typical core–rim compositional profiles are presented in Fig. 3A. They show irregular-shaped Ca- and Ti-richer dark cores with excess of alkalis in the [A] site, surrounded by intermediate and rim zones with higher Na^B and Fe^{3+} and lower Fe^{2+} contents. Decreasing Al with almost constant $(Na + K)^A$ contents yield increasing (Na + K)/Al ratios from cores to rims (Fig. 4C and D).

In general, post-magmatic riebeckite is homogenous; in the deformed facies it contains relatively high Zr contents (up to 0.03 apfu or 0.4 wt.% ZrO_2).

Much of the compositional variations for the amphiboles within the Papanduva pluton are related to coupled substitution reactions described by Giret et al. (1980), Strong and Taylor (1984), Hawthorne et al. (1994), Brown and Tocher (1982) and Duggan (1988), among others. These can be summarized in the following equations:

$$[Ca]^B + [Na]^A + 5[Fe^{2+}, Mn, Mg, Zn]^C + Si \leftrightarrow [Na]^B + [Li]^C + 4[Al, Fe^{3+}]^C + [Al]^T + []^A, \quad (1)$$

for the main components, and

$$2[Ti, Zr]^C + [Mg, Fe^{2+}, Mn, Zn]^C + [Al]^T \leftrightarrow 3[Al, Fe^{3+}]^C + Si, \quad (2)$$

that accounts for Ti and Zr substitution into the amphibole structure, which are always positively correlated in the samples investigated here; both reactions yield significant coefficients of determination (r^2) of 0.94 and 0.87, respectively (Fig. 4A and B).

Given the lack of calcic compositions, amphiboles define relatively short and evolved compositional trends in the diagram Ca + Al^{IV} vs. Si + Na + K (Fig. 5; after Giret et al., 1980). Amphibole in the massive facies records the broadest trend, from ferrorichterite to arfvedsonite compositions under progressively (alkali, Si)-rich and Ca-poor crystallization environments; in the foliated facies, arfvedsonite describes a narrow composition interval under (alkali, Si)-rich conditions. Late-stage, fine-grained, pristine arfvedsonite crystals and overgrowths approach the riebeckite end-member composition due to decreasing $(Na + K)^A$ and increasing Na^B.

5.2. Clinopyroxene

Aegirine I and III have compositions within the interval $Aeg_{82–99}Jd_{0–6}WEF_{0–13}$. Aegirine II is an almost pure aegirine ($Aeg_{93–97}Jd_{1–3}WEF_{2–5}$), while the aegirine–augite has compositions within $Aeg_{72–84}Jd_{1–2}WEF_{14–27}$. Aegirine I and III contain relatively high Ti (up to 0.2 apfu or 6.9 wt.% TiO_2) and Zr (up to 0.03 apfu or 1.4 wt.% ZrO_2) contents. Several crystal core compositions from the foliated facies (with Ti > 0.1 apfu) classify indeed as titanian aegirine (cf. Morimoto et al., 1988), and record the highest Ca abundances (up to 0.06 apfu or 1.6 wt.% CaO). Aegirine II contains relatively high, yet variable Mn (up to 0.03 apfu or 1.0 wt.% MnO) and Zn (up to 0.01 apfu or 0.4 wt.% ZnO) abundances.

Aegirine I and III depict the most significant and typical zoning patterns. A compositional profile for an aegirine I crystal from the foliated facies is displayed in Fig. 3B. The crystal has a dark-colored core (darker area in back-scattered electron image, BSE) surrounded by bright yellowish-green (lighter region in BSE image) intermediate and rim zones. Compositional variations record abrupt increases in Na and Fe^{3+} and decreases in Ca, Fe^{2+}, Mn, Ti, Zr, and less regularly Al abundances from core (titanian aegirine) to rims. However, as a whole, the clinopyroxene zoning patterns in the granites investigated here may be quite complex. For example, some aegirine I crystals from the deformed facies record opposite patterns, and Ti and Zr define both positive and negative correlations.

The aegirine–augite from the foliated and the massive facies are comparable, although Ca abundances span over a wide range (0.11–0.23 apfu or 2.7–5.6 wt.% CaO) in the former, and Zr contents are

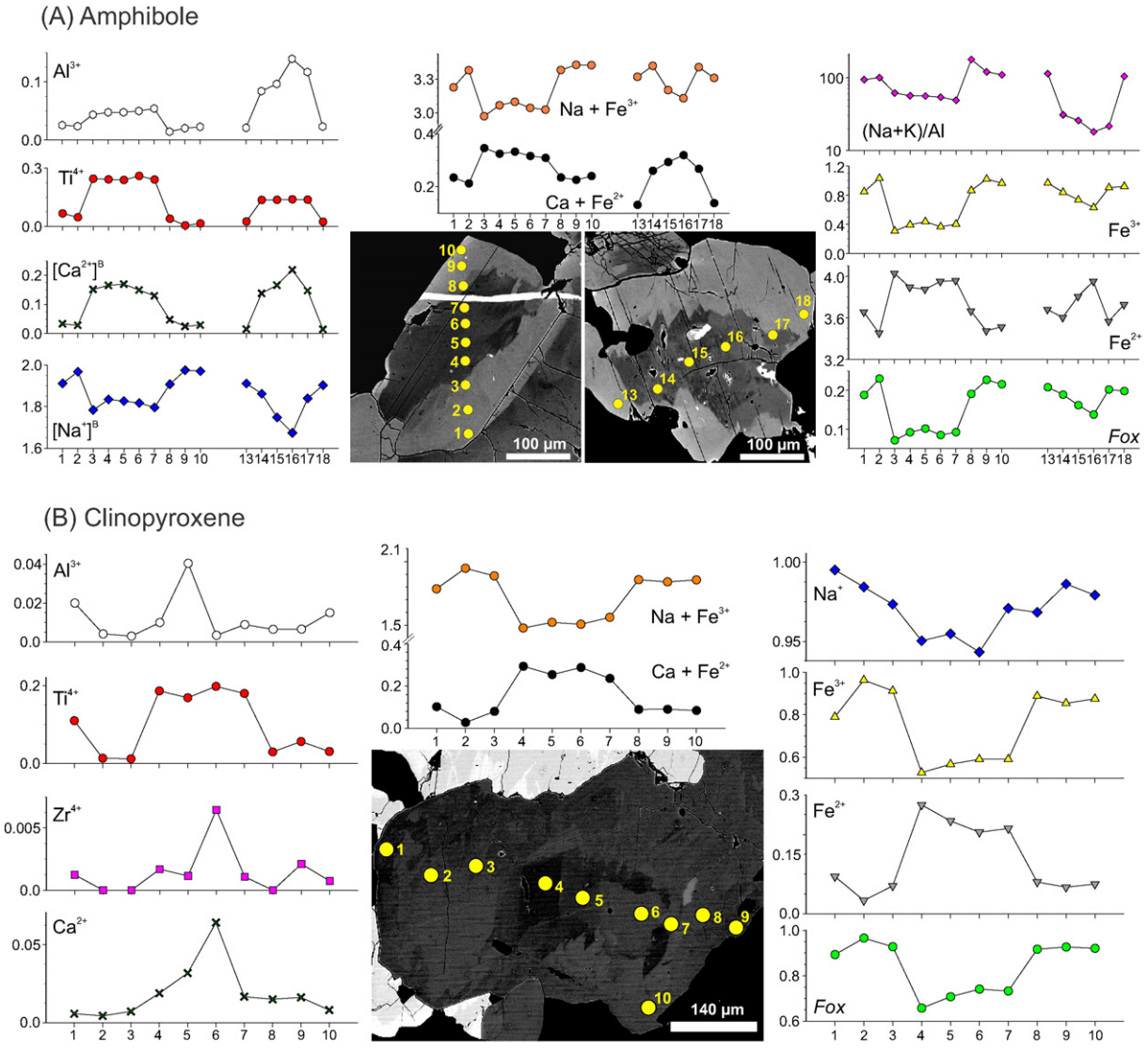

Fig. 3. Rim–core–rim cationic (apfu) profiles describing the main compositional variations in selected crystals of: (A) arfvedsonite from the foliated facies showing irregular zoning, as seen in the back-scattered electron images in compositional mode (BSE-Compo). Dark cores are Ti- and Na-rich, while bright rims are Na- and Fe^{3+}-rich; and (B) aegirine I from the foliated facies. Spot analyses are depicted in a BSE-Compo image of the crystal. Dark cores are Ti- and Na-rich, while bright rims are Na- and Fe^{3+}-rich. *Fox* = $Fe^{3+}/(Fe^{3+} + Fe^{2+})$.

among the highest measured (up to 0.02 apfu or 1.3 wt.% ZrO_2) in the latter.

Compositional variations in the Papanduva clinopyroxenes can be partially described by the substitution reaction relating Na–Ca pyroxenes (e.g., Deer et al., 2013):

$$[Na]^{M2} + [Fe^{3+}]^{M1} \leftrightarrow [Ca]^{M2} + [Fe^{2+}, Mn, Mg]^{M1} \quad (3)$$

Two distinct trends related to this reaction are recognized (Fig. 6). *Trend 1* correlates compositional variations between Na- and Fe^{3+}-poor titanian aegirine (crystal cores) and late- to post-magmatic aegirine (aegirine I, II and III); *trend 2* better conforms to the Ca-rich aegirine cores with aegirine–augite compositions. Both trends are better modeled considering the NAT ($NaTi_{0.5}Fe_{0.5}Si_2O_6$) and NAZ ($NaZr_{0.5}Fe_{0.5}Si_2O_6$) molecules in the (Aeg + Jd)–(NAT + NAZ)–(Di + Hd) plot (Fig. 7A), where trend 1 defines a pathway of decreasing NAT + NAZ combined with increasing Aeg + Jd contents from core to crystal rims at constant Hd + Di (Fig. 7B); a compositional gap does exist between titanian aegirine cores and aegirine I to III (Fig. 7A). Trend 2 is characterized by a subtle increase in Di + Hd that ultimately gives rise to aegirine–augite compositions with NAT + NAZ contents that partially fill in the aforementioned gap.

6. Trace element compositional variations

In this section, the median compositions of amphiboles and clinopyroxenes are reported and discussed rather than individual spot analyzes. Medians are preferred since the concentrations of some trace elements exhibit a large range, even when considering crystals belonging to the same textural generation. The complete LA-ICP-MS data set and some related basic statistics are available as supplementary material.

6.1. Amphibole

Trace element and rare earth element (REE) chondrite normalized patterns for ferrorichterite, arfvedsonite, and riebeckite are shown in Fig. 8A and B, respectively. Arfvedsonite has higher concentrations of Rb and U (Large Ion Lithophile Elements — LILE), Nb, Ta, Zr, and Hf (HFSE), as well as Li and Zn. REE patterns record an enrichment of HREEs ($0.04 \le La_N/Yb_N \le 0.5$) with a well-developed negative Eu anomaly [$0.1 \le Eu/Eu^* \le 0.2$; where $Eu^* = (Sm_N * Gd_N)^{0.5}$].

Ferrorichterite is characterized by relatively enriched trace element compositions and REE chondrite normalized concentrations that are 3- to 4-fold higher than those for sodic amphiboles. REE patterns are

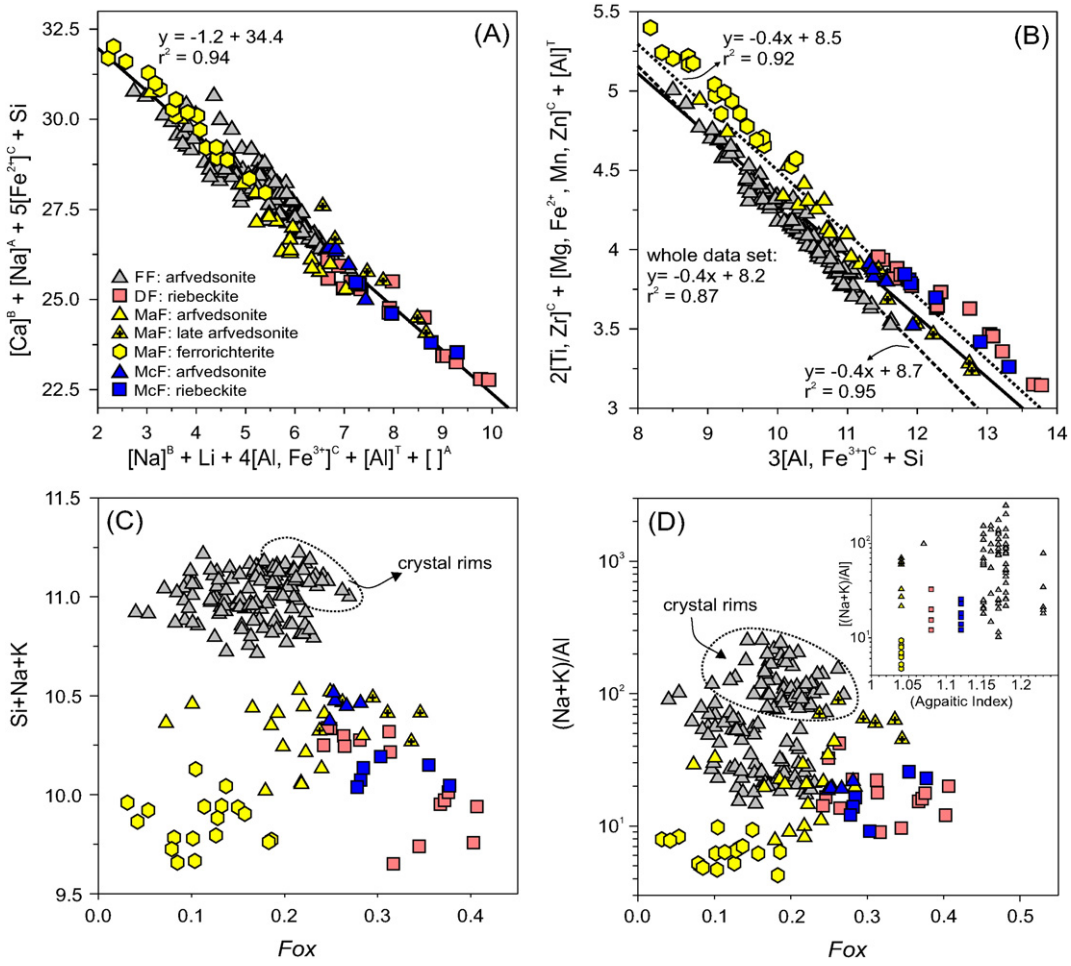

Fig. 4. Binary plots showing compositional variations (apfu) of amphibole from the Papanduva Pluton. (A) Cationic plot $[Na]^B + Li + 4[Fe^{3+}]^C + [Al]^T + [\ ]^A$ versus $[Ca]^B + [Na]^A + 5[Fe^{2+}]^C + Si$, Si, with Li contents estimated from the LA-ICP-MS analysis. (B) Cationic plot $3[Al, Fe^{3+}]^C + Si$ versus $2[Ti, Zr]^C + [Mg, Fe^{2+}, Mn, Zn]^C + [Al]^T$. (C) Cationic *Fox* $[Fe^{3+}/(Fe^{3+} + Fe^{2+})]$ versus Si + Na + K plot. (D) Cationic *Fox* versus (Na + K)/Al plot. Inset depicts how (Na + K)/Al ratio in amphiboles correlates with the Agpaitic Index (AI) of the host rock. Note grouping of crystal rim compositions, especially in terms of the (Na + K)/Al ratio. FF: foliated facies; DF: deformed facies; MaF: massive facies; McF: micrograniticfacies.

flat through the LREEs, with relative HREE enrichment ($0.1 \le La_N/Yb_N \le 1.1$) and a similar negative Eu anomaly ($0.11 \le Eu/Eu^* \le 0.15$).

Riebeckite is depleted in most of the LILEs, HFSEs (mainly Nb-Ta and Zr-Hf), and transition metals (Fig. 8A). REE patterns indicate a relative enrichment of HREEs ($0.1 \le La_N/Yb_N \le 0.2$), in particular from Ho to Lu and a similar negative Eu anomaly.

Trace element zoning patterns are not as straightforward as those described for the major and minor elements for most of the analyzed crystals. Nevertheless, they are well defined in some arfvedsonite crystals from the deformed facies, where decreasing LILE, HFSE, as well as Sn, Li, transition metals, and REE contents are recorded from core to rims.

6.2. Clinopyroxene

Trace element and REE chondrite normalized patterns for aegirine and aegirine–augite are shown in Fig. 9. Aegirine I from the foliated granites has relatively low LILE and high HFSE contents, especially Nb and Ta abundances. The highest LILE abundances were measured in the massive granites, while the highest Zr contents were determined for the microgranites. In contrast, aegirine II records the highest transition metals (mainly Zn) concentrations. Significant negative anomalies for Pb, Sr, and transition metals, and a slight depletion for Li are common features of aegirine from all petrographic facies (Fig. 9A)

REE patterns for aegirine I define a pronounced enrichment of HREEs ($0.02 \le La_N/Yb_N \le 0.8$ and) and a significant negative Eu anomaly ($0.1 \le Eu/Eu^* \le 0.4$). A remarkable contrast in the REE patterns is present between crystals from the foliated and massive granites relative to those from the deformed granites and microgranites. LREE patterns for aegirine I from the foliated and massive facies display a discrete concave shape, while crystals from the deformed granites and microgranites reveal a steeply-rising slope through the LREEs and higher abundances for the middle REEs (Gd-Dy; Fig. 9C).

As with the amphiboles, trace element zoning patterns in the clinopyroxenes are discrete when compared to their major and minor elemental abundances. Aegirine I from the foliated granites exhibit decreasing LILE and LREE abundances, and heterogeneous HFSE variations towards crystal rims.

The Mn-rich aegirine II REE patterns also define a strong enrichment of the HREEs ($0.4 \le La_N/Yb_N \le 0.6$) and a distinct, steeply negative slope through the LREEs. Of note, Olin and Wolff (2010) have suggested that Mn plays an important role in controlling the HREE enrichment in pyroxenes.

Aegirine III from the foliated and massive facies shows distinct trace element and REE patterns (Fig. 9B and D). Crystals from the foliated facies record higher abundances for most of the elements. Of note, Li does not show a significant depletion as exhibited by both aegirine I and II, whereas Zr and Hf abundances are among the highest observed. REE

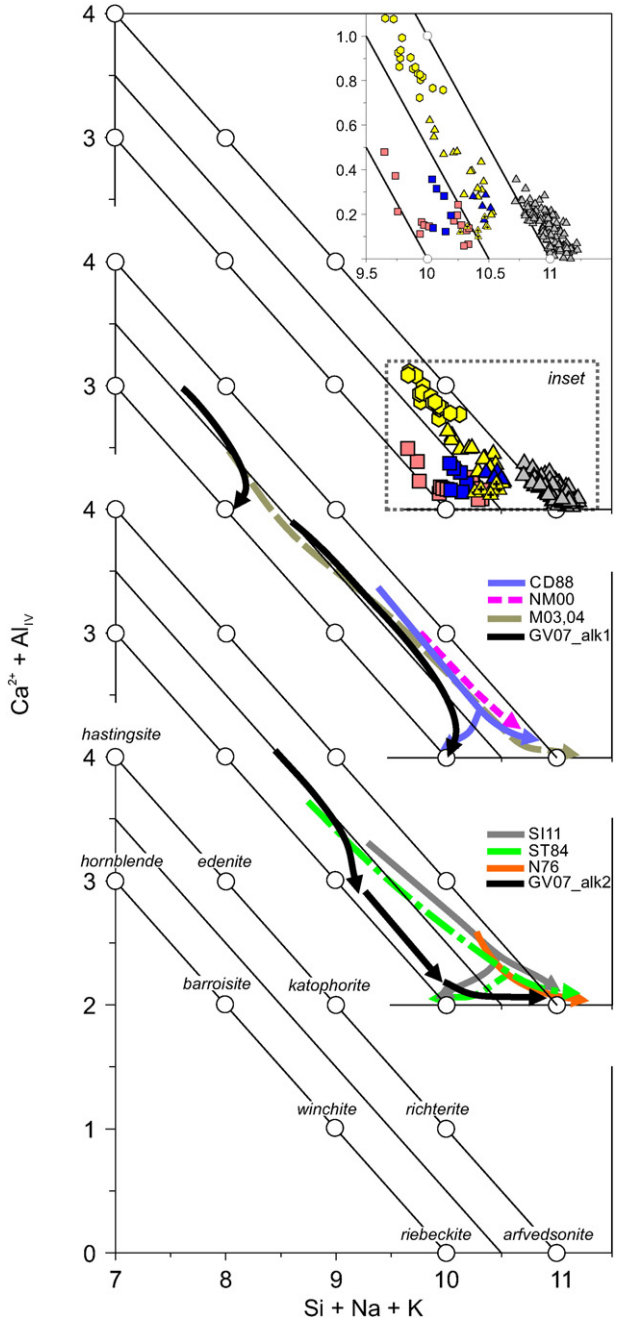

Fig. 5. Cationic Si + Na + K versus Ca + Al^{IV} plots (apfu) for amphibole from the Papanduva Pluton and compositional trends for interesting localities worldwide, including other plutons from the Graciosa Province. CD88: Virgin Canyon Pluton (Czamanske and Dillet, 1988); NM00: Pandé Massif (Njonfang and Moreau, 2000); M03,04: Puklen Complex (Marks et al., 2003, 2004); GV07_alk1: Serra da Graciosa Alkaline Association 1, Graciosa Province (Gualda and Vlach, 2007b); SI11: Emeishan Province (Shellnutt and Iizuka, 2011); ST84: Topsails and St. Lawrence Complexes (Strong and Taylor, 1984); N76: Oslo Rift (Neumann, 1976); GV07_alk2: Serra da Graciosa Alkaline Association 2, Graciosa Province (Gualda and Vlach, 2007b). All data were recalculated following the procedures described in Appendix A. Symbols as in Fig. 4.

contents are up to two orders of magnitude higher, with flatter patterns in the LREE region and a discrete HREE enrichment ($0.1 \le La_N/Yb_N \le 0.4$). Crystals from the massive facies show a steeply-rising slope through the LREEs, with a relative Ce depletion, and strong enrichment in the HREEs ($0.05 \le La_N/Yb_N \le 0.3$).

Aegirine–augite exhibits the most contrasted trace element and REE patterns (Fig. 9B and D). Most HFSEs abundances are depleted when compared to those for aegirine, but higher LILE abundances and a

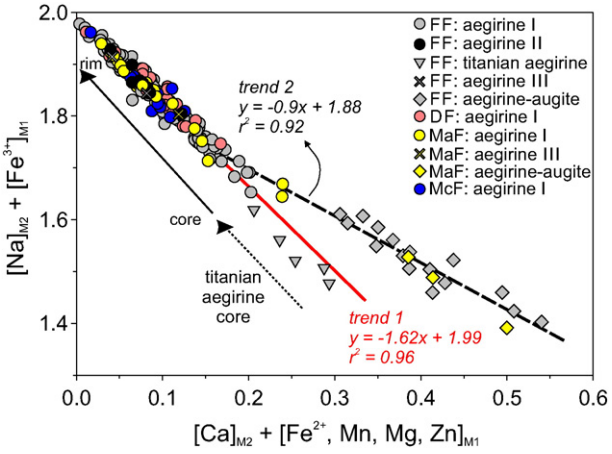

Fig. 6. Cationic $[Ca]^{M2} + [Fe^{2+}, Mn, Mg, Zn]^{M1}$ versus $[Na]^{M2} + [Fe^{3+}]^{M1}$ plot (apfu) for clinopyroxene from the Papanduva Pluton. FF: foliated facies; DF: deformed facies; MaF: massive facies; McF: microgranitic facies.

strongly developed positive Li anomaly are notable. REE concentrations are up to two orders of magnitude lower when compared to aegirine; its patterns exhibit a relative LREE enrichment over HREE ($2.7 \le La_N/Sm_N \le 3.3$). They are flatter, though with some dispersion in the HREE region, which may be related to the low measured concentrations (REE = 15–31 ppm; HREE = 1.4–2.5 ppm) and consequently large associated uncertainties.

7. Oxygen isotope data

Oxygen isotopic analyses were obtained for the best available samples representative of the main petrographic facies. The calculated $\delta^{18}O$ values relative to VSMOW are shown in Fig. 10 and listed in the supplementary materials. Measurements were made on ferrorichterite, aegirine, and quartz triplets, and ferrorichterite and quartz pairs of the massive facies (samples MR-89 and MR-39, respectively); arfvedsonite, aegirine, and quartz triplets from the foliated facies (sample MR-21, relatively coarse-grained, and MR-03, fine-grained and highly deformed); aegirine and quartz from the microgranite (MR-01D), and aegirine and quartz (MR-47B, deformed facies) pairs. In general, $\delta^{18}O$ values are systematically lower in the massive granites compared to the foliated facies, ranging from 2.3‰ to 6.4‰ for amphiboles and aegirine, and between 7.3‰ and 10.1‰ for quartz. The oxygen isotope compositions for crystals from deformed granites and microgranites yielded intermediate values.

Individual $\delta^{18}O$ values for quartz progressively increase from 7.3 to 10.1‰, in the order: massive, microgranitic, deformed, and foliated petrographic facies, respectively; sample MR-39, which has an O isotope value similar to that for the sample MR-47B, is the exception. Within the foliated facies, quartz $\delta^{18}O$ values increase with deformation and/or degree of recrystallization, from sample MR-21 (9.2‰) to MR-03 (10.1‰). For samples in which ferrorichterite/arfvedsonite, aegirine and quartz were analyzed, all of them show increasing $\delta^{18}O$ values from the massive to the foliated facies, and within the latter, $\delta^{18}O$ values are much higher in the most deformed sample. Samples from the massive (MR-39) and microgranitic (MR-01D) facies with single analyzed aegirine–quartz or riebeckite-quartz pairs, respectively, depart to some extent from this trend, as both aegirine and riebeckite record relatively high $\delta^{18}O$ values. Of note, textural evidences suggest that riebeckite in sample MR-01D is a typical post-magmatic phase, and that there was significant late-stage re-equilibration in sample MR-47B, with crystallization of post-magmatic riebeckite and magnetite closely related to aegirine formation.

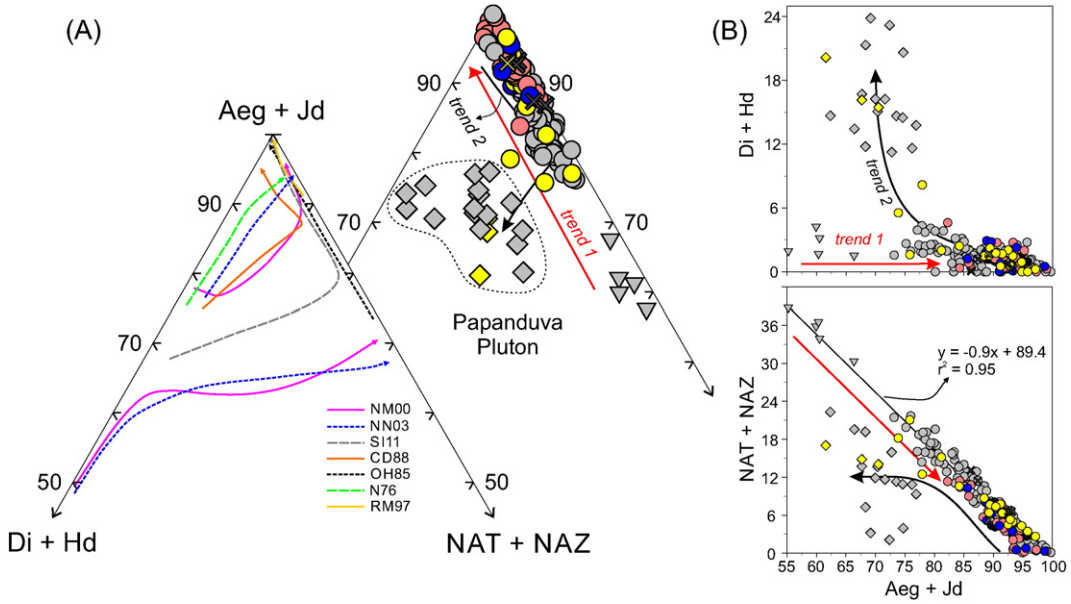

Fig. 7. Compositional variations in terms of molecular contents (%) of clinopyroxene from the Papanduva Pluton. (A) Ternary molecular Aeg + Jd versus NAT + NAZ versus Di + Hd plots for the Papanduva Pluton and compositional trends for interesting localities worldwide. NM00: Pandé Massif (Njonfang and Moreau, 2000); NN03: Cameroon Line (Njonfang and Nono, 2003); SI11: Emeishan Province (Shellnutt and Iizuka, 2011); CD88: Virgin Canyon Pluton (Czamanske and Dillet, 1988); OH85: Ras ed Dom Ring Complex (O'Halloran, 1985); N76: Oslo Rift (Neumann, 1976); RM97: Strange Lake Complex (Roelofsen and Martin, 1997). (B) Binary molecular plots Aeg + Jd versus NAT + NAZ and Aeg + Jd versus Di + Hd. Molecules: Aeg — aegirine; Jd — jadeite; Di — diopside; Hd — hedenbergite; NAT — $NaTi_{0.5}(FM)_{0.5}Si_2O_6$; NAZ — $NaZr_{0.5}(FM)_{0.5}Si_2O_6$. Symbols as in Fig. 6.

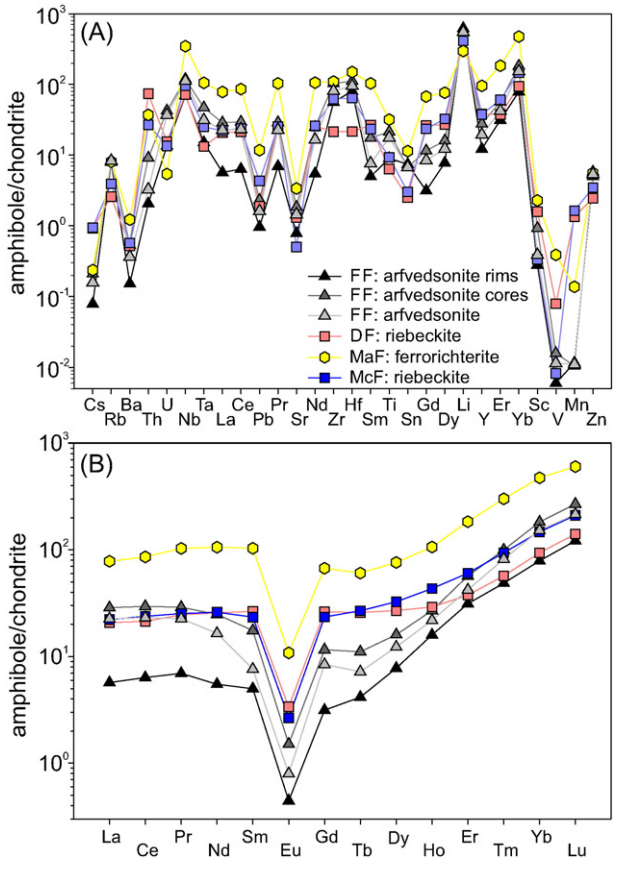

Fig. 8. Median chondrite-normalized trace element (A) and rare-earth patterns (B) for amphibole from the Papanduva Pluton normalized to the chondrite values of McDonough and Sun (1995). FF: foliated facies; DF: deformed facies; MaF: massive facies; McF: microgranitic facies.

8. Discussion

8.1. Late- and post-magmatic evolution trends

8.1.1. Amphibole

The magmatic and subsolidus evolution trends for amphibole from the Papanduva pluton are described in Fig. 5, and are compared to other alkaline siliceous rock occurrences including other plutons within the Graciosa Province. In particular, the amphibole compositional variations for the massive facies are compared to the oxidation trends of Strong and Taylor (1984), and are consistent with those for peralkaline siliceous rocks from the Questa Caldera, New Mexico (Czamanske and Dillet, 1988), and those for peralkaline granites from the Emeishan Province, China (Shellnutt and Iizuka, 2011) (Fig. 5). In fact, *Fox* [$Fe^{3+}/(Fe^{2+} + Fe^{3+})$] ratios and peralkalinity increase from ferrorichterite to arfvedsonite. Riebeckite from the deformed and microgranitic facies shows the highest *Fox* values (Fig. 4C); this and the associated textures suggest it formed by alteration of the primary Na- and Na–Ca amphiboles in a post-magmatic, relatively higher oxidizing environment; a finding in agreement with Ernst (1962; see also Mitchell, 1990) who showed that riebeckite is unstable at magmatic conditions.

Arfvedsonite cores from the protomylonitic facies show a limited evolution path in part comparable to the magmatic-subsolidus trend under reducing conditions of Strong and Taylor (1984). Their compositions partially overlap those found in the Pandé Massif, Cameroon Line (Njonfang and Moreau, 2000), and in the "group 3" amphiboles of granites and syenites from the Oslo Rift (Neumann, 1976) where crystallization took place under reducing conditions. However, Hawthorne et al. (1993) invalidated the assumption of an universal reducing environment for development of compositional trends occurring under magmatic-subsolidus conditions. Hawthorne et al. (1993) argue that if the Strong and Taylor's (1984) trends take into consider the substitution of Li^+ into the amphibole structure ($Li_{-1}Fe^{3+}_{-1}Fe^{2+}_{2}$), then these can be far more oxidizing than the designated, typical oxidizing trend. Furthermore, Marks et al. (2011) showed that at sufficiently high aNa_2O, arfvedsonite (along with aegirine) occurs in both reducing and oxidizing conditions. The arfvedsonite in the foliated facies has Li contents up to 1.5 wt.% (see supplementary material) and its highest *Fox* values

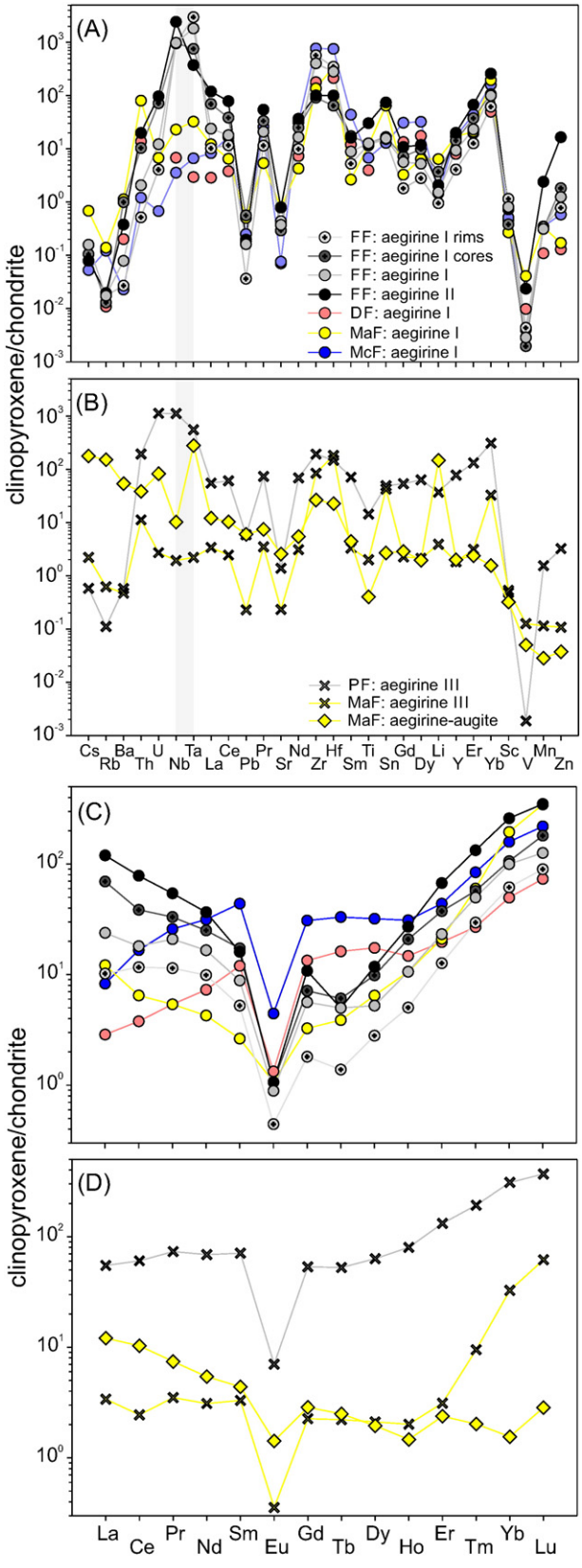

Fig. 9. Median chondrite-normalized trace element and rare-earth patterns for late-magmatic (A and B) and late- to post-magmatic clinopyroxene (C and D) from the Papanduva Pluton, normalized to the chondrite values of McDonough and Sun (1995). FF: protomylonitic facies; DF: cataclastic facies; MaF: massive facies; McF: microgranitic facies.

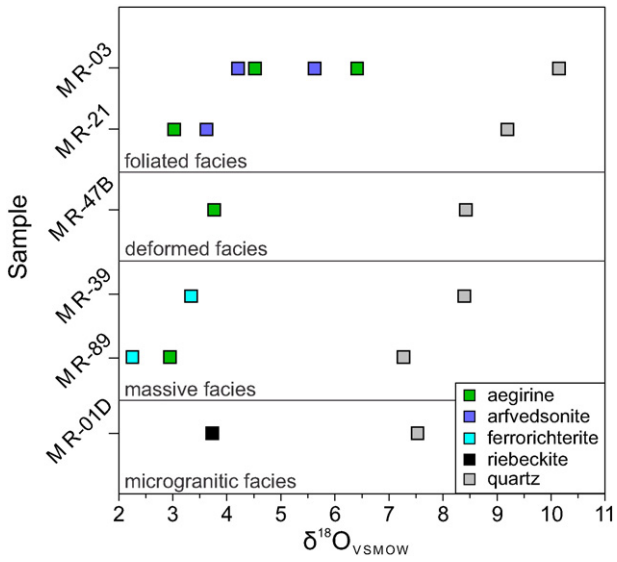

Fig. 10. Oxygen isotope composition of amphibole, clinopyroxene, and quartz separates from the Papanduva Pluton.

(up to 0.27) overlap some of those found in riebeckite (Fig. 4C). Based on these evidences, crystallization of arfvedsonite cores most probably occurred under oxidizing rather than truly reducing environments.

Compared to their corresponding cores, arfvedsonite rim compositions define a subtle increase in both peralkalinity ((Na + K)/Al), which correlate positively with the host-rock Agpaitic Index (cf. Giret et al., 1980) and *Fox* oxidation ratios (Fig. 4D). Markl et al. (2010) demonstrate that peralkalinity is closely associated with fO_2, and controlled by the coupled substitution mechanisms involving $Na + Fe^{3+}$ in both arfvedsonite and aegirine (Figs. 4 and 6). Therefore, we suggest that arfvedsonite crystallized in two different stages. Crystal cores precipitated first under slightly lower activities of alkalis and O_2. This stage was followed by increases in the alkali activity and *Fox* oxidation ratio within the system, which promoted disequilibrium conditions and observed core resorption textures, and subsequent crystallization of Na- and Fe^{3+}-rich rims (Fig. 4C and D). Such increases in alkalinity or oxidation can be related to either degassing episodes within the crystallizing chamber or, as will be discussed later, to melt-present deformation events.

Arfvedsonite, in particular that formed during the late crystallization stages, define a significant positive correlation between Ti and Zr abundances and oxidation ratios, which corroborates the notion that the incorporation of both elements into the amphibole structure is clearly favored by high oxidizing and peralkaline conditions.

8.1.2. Clinopyroxene

Papanduva main clinopyroxenes are marked by narrow compositional intervals and typical geochemical features, such as the enrichment in both Na and Fe^{3+} and depletion in Ca and Fe^{2+} contents, at constant Na/Fe^{3+} ratios of ~1.0. As displayed in Fig. 7A, the Ca- and Fe^{2+}-poor, late- to post-magmatic evolution trend 1 (aegirine I to III) partially overlaps that defined by clinopyroxenes of A-type granites from Ras ed Dom (O'Halloran, 1985) and Strange Lake (Roelofsen and Martin, 1997) complexes, respectively. Contrarily, trend 2 defines a subtle increase in Ca and Fe^{2+} contents during post-magmatic stages that ultimately gives rise to aegirine–augite compositions (Fig. 7B). Of interest, this trend is opposite to those commonly described in worldwide occurrences (Fig. 7A), such as in the peralkaline rocks from the Emeishan Province, China (Shellnutt and Iizuka, 2011) and Pandé Massif, Cameroon (Njonfang and Moreau, 2000).

The occurrence of Ti-/Zr-rich clinopyroxene, as found in the deformed facies, is a well-known feature of felsic alkaline rocks

(e.g., Nielsen, 1979; Njonfang and Nono, 2003; Dyulgerov and Platevoet, 2006). This type of enrichment has been attributed to several factors, including melt composition, lack of concurrent Ti/Zr-bearing minerals, and O_2 activity. Both Gwinn and Hess (1989) and Keppler (1993) demonstrated that alkalis- and F-excess in melts/liquids increase Zr and Ti solubilities, whereas Njonfang and Nono (2003 and references therein) point out that low fO_2 favors the crystallization of titanian and/or zirconian aegirine. Aegirine from the Papanduva pluton preferentially incorporates Ti and Zr into the Ca-rich crystal cores with low *Fox* ratios (true titanian aegirine compositions), and their contents decrease towards the alkali-rich crystal rims with high *Fox* ratios (e.g., Figs. 3B, 6, and 7B). Therefore, it seems that the distribution of Ti and Zr can be related to both alkali activity and redox conditions of the late- to post-magmatic liquids and fluids. However, in the case of the Papanduva foliated facies, the coeval crystallization of competing HFSE-bearing rare accessory minerals have certainly also played a role in controlling Ti and Zr budgets.

8.2. Trace element partition and controls

There is a lack of textural evidence that indicates equilibrium crystallization of amphibole and clinopyroxene in the Papanduva Pluton, thus partitioning estimates for trace elements between these minerals would yield poor modeling results. Nevertheless, arfvedsonite and aegirine share analogous evolution trends, in particular the increase in Na and Fe^{3+} contents towards crystal rims. Similarly, these minerals may also define similar trace element compositional variations, mainly for Rb, Sr, Eu, V–Co, Zr–Hf, and REEs.

As shown in Section 6, trace element and REE patterns define systematic decreases in LILEs, HFSEs, and especially REE from ferrorichterite to arfvedsonite. Marks et al. (2004) report a continuous decrease in LREE contents from Ca-rich amphibole and clinopyroxene relative to their Na-rich counterparts in the Ilímaussaq Complex; a feature attributed to the fractionation of REE-bearing accessory minerals, such as eudialyte. Similarly, the observed REE- and HFSE-depletions in our amphibole, in particular towards crystal rims and late-crystallizing phases (Fig. 8), may be linked to the beginning of crystallization of late- to post-magmatic competing REE- and HFSE-bearing accessory minerals. In this study, it includes britholite-(Ce), nacareniobsite-(Ce), (Na–K)-zirconosilicates and narsarsukite, among others, which are typical in the foliated facies. Late-stage crystallization of aegirine I may also have exerted some control, as evidenced by the systematic decrease of Sc concentrations from ferrorichterite to arfvedsonite (Fig. 8A), and within a single arfvedsonite crystal from core to rim (e.g., Mahood and Hildreth, 1983).

The fact that aegirine crystallizes after amphibole argues for an increase in fO_2 conditions during late- to post-magmatic stages (cf. Njonfang and Moreau, 2000). In such a scenario, the composition of clinopyroxene and associated intra-crystalline chemical variations seem to be mainly influenced by the composition of the residual peralkaline liquids (e.g. Ferguson, 1978; Grapes et al., 1979) rather than by crystal-chemical effects. The distribution of both Nb and Ta serve to illustrate such an interpretation (Fig. 9A and B): the relatively lower degree of HFSE enrichment in clinopyroxene when transitioning from the deformed, microgranitic, and massive facies is consistent with available inter-mineral partition coefficient data that consistently demonstrate the greater preference of pentavalent HFSEs for the amphibole structure (e.g., Zack et al., 1997; Marks et al., 2004; Reguir et al., 2012 and references therein). However, it cannot explain the higher Nb and Ta contents in the aegirine from the foliated facies, which sometimes are higher than those recorded in amphibole (Figs. 8A and 9A). In this case, HFSE-rich residual liquids or fluids exert a major influence on the final compositions of clinopyroxene.

Trace element compositions reported for aegirine–augite (Fig. 9B and D) were obtained for crystals solely from the massive facies since adequate grains for laser ablation experiments were not found in the remaining samples due mainly to crystal size considerations. However, based on the similar textural context and major element compositional variations, it is assumed that aegirine–augite from both massive and foliated facies most likely display similar trace element behavior since it is a post-magmatic phase in both units that was not affected by late-stage events.

Aegirine–augite crystallized subsequent that of aegirine and that of a variety of rare HFSE- and REE-bearing accessory minerals, including, among others, zircon in the massive facies, and elpidite and other (Na,K)-bearing zirconosilicates in the foliated facies. These minerals are characterized by high HREE abundances (up to 5600 ppm in zircon, and 120,000 ppm in zirconosilicates) and a strong enrichment of the HREEs over the LREEs (unpublished data), which explain the typical HREE-depleted patterns observed in aegirine–augite (Fig. 9D). The behavior of Li in clinopyroxene is also intriguing (cf. Fig. 9A and B). Marks et al. (2004) concluded that Li partitioning in clinopyroxene from the Gardar Province (Greenland) is mainly controlled by the composition of coexisting liquids and that Li strongly prefers amphibole structures (see also Hawthorne et al., 1993, 1994). In the Papanduva granites, aegirine–augite records a significant positive anomaly for Li (Fig. 9B), while aegirine that formed from late-stage, residual magmatic melts that have previously crystallized amphiboles define the opposite behavior (Fig. 9A). Hence, at truly post-magmatic stages not influenced by the crystallization of amphibole, Li may indeed substitute into the aegirine–augite structure.

8.3. REE partition controls

The REE patterns for the most Na–Fe^{3+}-enriched amphibole and clinopyroxene (Figs. 8B and 9C) define a V-shape typical of those occurring in alkaline and peralkaline siliceous and undersaturated rocks (e.g. Marks et al., 2004; Reguir et al., 2012). This suggests that REEs are incorporated in two crystallographic sites with different optimal cation radii (cf. Bottazzi et al., 1999; Reguir et al., 2012); a finding in disagreement with the lattice-site elastic-strain model (LSM; Blundy and Wood, 1994, Wood and Blundy, 1997), which assumes complete REE ordering into a single site. Of note, Marks et al. (2004) also demonstrated that partition coefficients derived either from natural samples, or from LSM modeling do not yield reliable melt compositions when dealing with such minerals.

The data reported here lead to similar conclusions, except for aegirine–augite, which accommodates satisfactorily all REEs into the eight-fold coordinated M2 site. In fact, calculated REE mineral/melt partition coefficients ($^{min/L}D_{REE}$) for amphibole and clinopyroxene (see supplementary material) reveal that REEs cannot be fitted to a single near-parabolic curve in Onuma-type diagrams; rather they selectively fill in distinct crystallographic sites (Tiepolo et al., 2007; Olin and Wolff, 2010; Reguir et al., 2012). Thus, following Bottazzi et al. (1999), Olin and Wolff (2010) and Reguir et al. (2012), the calculated $^{amph/L}D_{REE}$ and $^{cpx/L}D_{REE}$ were adjusted according to the LSM by ordering the LREEs (La-Tb) into eight-fold coordinated sites (M4 in amphibole, M1 in clinopyroxene), and the HREEs (Dy-Lu) and Sc into the six-fold coordinated sites (M2 in amphibole, M1 in clinopyroxene).

The results show a decreasing REE compatibility from ferrorichterite to arfvedsonite (Fig. 11A); the fitted curves are similar for the HREEs but somewhat distinct for the LREEs, highlighting a steep increase from La to Nd (especially in riebeckite) and a slight increase from Sm to Tb. The most Na–Fe^{3+}-rich arfvedsonite from the foliated facies records the lowest LREEs compatibility; $^{cpx/L}D_{LREE}$ values describe a smooth, almost symmetric parabolic curve centered at a radius of ca. 1.02 (see Fig. 11A). For clinopyroxene, the calculated $^{cpx/L}D_{LREE}$ define distributions comparable to those for amphiboles for the massive, deformed, and microgranitic facies, and there is a decreasing HREE compatibility from aegirine I crystals of the massive to those from the foliated facies (Fig. 11B). In contrast, $^{cpx/L}D_{LREE}$ values for aegirine of the foliated facies indicate a distinct decreasing trend for the LREEs from Ca-rich cores to

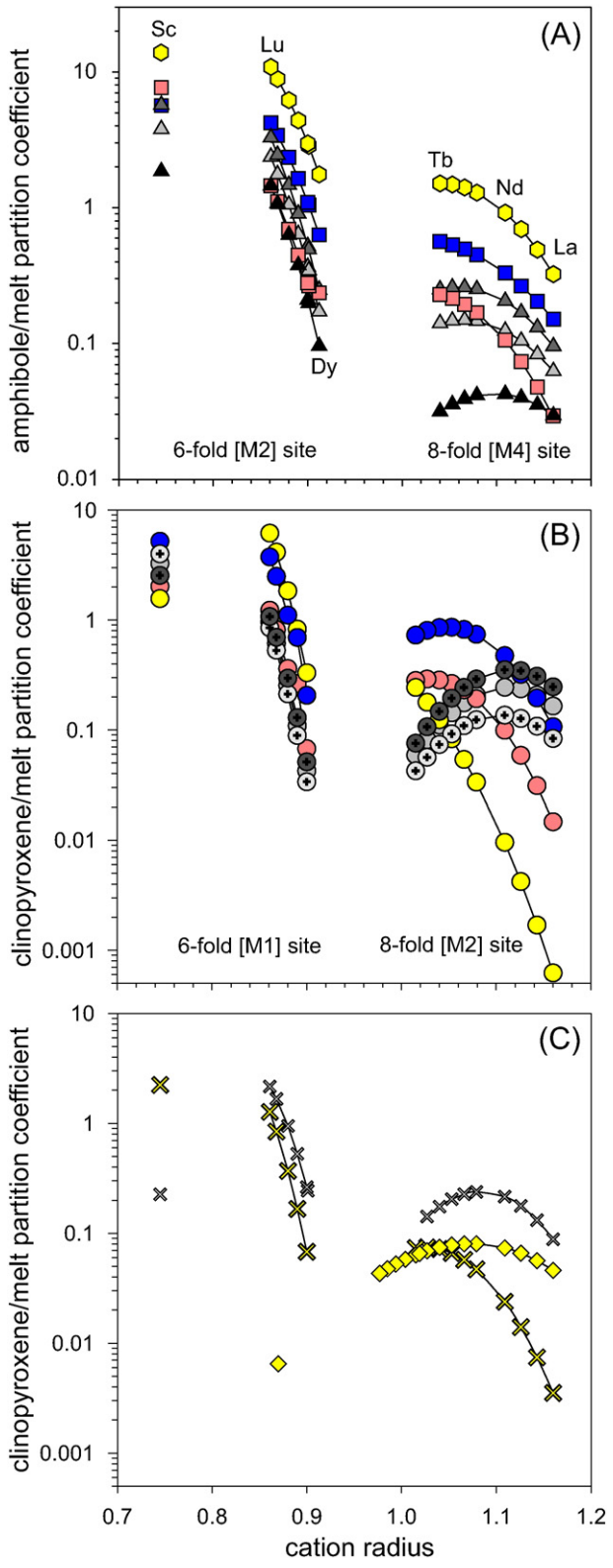

Fig. 11. Mineral-melt partition coefficients calculated from representative mineral chemical data according to the Lattice Strain Model (LSM). (A) Amphibole-melt REE and Sc^{3+} partition coefficients calculated at P = 100 MPa and T = 700 °C, considering LREE and HREE partition into two different crystallographic sites. (B) Late-magmatic and (C) late- to post-magmatic clinopyroxene-melt REE and Sc^{3+} partition coefficients calculated at P = 100 MPa and T = 600 °C, considering LREE and HREE partition into two different crystallographic sites, except for aegirine–augite. Symbols in (A) as in Fig. 8; symbols in (B) and (C) as in Fig. 9.

Na–Fe^{3+}-rich rims (Fig. 11B). $^{cpx/L}D_{REE}$ for aegirine III display similar distributions relative to aegirine I, while aegirine–augite, as stated above, defines a smooth distribution with all REEs filling in M2 sites (Fig. 11C; Wood and Blundy, 1997).

These findings suggest a crystal-chemical control, especially the role of Ca^{2+} on the $^{min/L}D_{REE}$ distribution patterns; however, the influence of the composition and structure of the crystallizing melts or fluid phases cannot be ruled out (e.g., Prowatke and Klemme, 2005) as also suggested earlier in order to explain the trace element behavior. Thus, the dependence of the calculated D_{REE} values relative to melt composition for amphibole and aegirine I can be tested using the corresponding host-rock AI and ASI values. A systematic decrease in the overall magnitude of the partition coefficients (D_0 in the LSM equation, cf. Blundy and Wood, 1994) towards higher AI and lower ASI values for both LREEs and HREEs is observed in amphibole, whereas in aegirine I, $^{cpx/L}D_{LREE}$ increases and $^{cpx/L}D_{HREE}$ decreases, respectively.

The REEs substitution in common pyroxene structures may be described by the reaction $^{T}Si + [R^{2+}]^{M2} \leftrightarrow [Al^{3+}]^{T} + [REE^{3+}]^{M2}$ ($R^{2+} = Fe^{2+}$, Mg^{2+}, Mn^{2+}), and depends on its Al content which in turn is influenced by melt composition and structure (e.g., Shearer et al., 2006). However, Na–Fe^{3+}-rich pyroxene and amphibole typically exhibit relative HREE enrichment and LREE depletion (Marks et al., 2004; Schilling et al., 2011; Piilonen et al., 2013). This indicates a major crystal chemical control on REE partitioning, especially the preference of trivalent REEs to charge-balance Na^{+} incorporation by the reaction $Na^{+} + REE^{3+} \leftrightarrow 2Ca^{2+}$ involving the smaller $^{[8]}$M2 site (Wood and Blundy, 1997). Hence, it is expected that HREEs rather than LREEs are more compatible in Na–Fe^{3+}-rich pyroxene compositions.

In this study, the opposite trend is observed as both the LREEs and HREEs are more compatible in magmatic amphiboles from rocks with higher ASI values (and within a precipitating crystal in the Al- and Ca-rich cores), suggesting a significant influence by the melt composition. In fact, a higher Al content in the melt enhances REEs (+Al) incorporation into the amphibole structure according to:

$$Si + Fe^{3+} + Na \leftrightarrow Al^{IV} + REE + Ca. \quad (4)$$

During late- to post-magmatic stages under oxidizing conditions and high peralkalinity (e.g. Fig. 4C and D), REEs tend to remain in the melts or fluids, allowing for the late precipitation of aegirine I and REE-rich accessory phases; these phases will therefore compete for the REEs, which appears to be the case for the foliated facies in the Papanduva Pluton. This may also explain the observed patterns of decreasing D_{REE} from cores to rims for aegirine I.

8.4. The replacement of amphibole by aegirine III

The replacement of arfvedsonite by late-stage aegirine is a well-known feature in peralkaline rocks. Previous studies have attributed it to a post-magmatic reaction involving peralkaline residual fluids under relatively high fO_2 and low temperatures (e.g. Grapes et al., 1979; Scaillet and MacDonald, 2001; Marks et al., 2003). According to Salvi and Williams-Jones (1990), aegirine mantles around amphibole result from hydrothermal alteration in the presence of a (Na, F)-rich and Ca-poor orthomagmatic fluids. In this study, the pertinent reactions:

$$Na_3Fe_5Si_8O_{22}(OH)_2 + Na_2Si_2O_5 + O_2 \leftrightarrow 5NaFeSi_2O_6 + H_2O, \quad (5)$$

and

$$Na_2CaFe_5Si_8O_{22}(OH)_2 + 1.5Na_2Si_2O_5 + O_2 \leftrightarrow 5NaFeSi_2O_6 + SiO_2 + Ca^{2+} + 1.5OH^{-} + 0.5H^{+} \quad (6)$$

explain very well the post-magmatic substitution of both arfvedsonite and ferrorichterite by aegirine III, respectively. In this case, aegirine III is relatively enriched in REEs and HFSEs when substituting for

arfvedsonite, but depleted in most elements when replacing ferrorichterite (Fig. 12). This indicates that the fluid phase composition exerts a strong control on the composition of aegirine III overgrowths, which is in agreement with the substitution scheme outlined in Eq. (4).

8.5. Role of deformation: oxygen isotope evidence

Oxygen isotope fractionation between mineral pairs from the studied samples ($\Delta_{qz-amph} = +3.8$ to $+5.6$‰) and quartz–aegirine ($\Delta_{qz-aeg} = +3.7$ to $+6.2$‰) are relatively high. Consequently, low apparent equilibrium temperatures (<450 °C) are obtained based on the fractionation factors of Zheng (1993a, 1993b) as shown in Fig. 13A. However, these results contrast with our independent temperature estimates based on the quartz c-axis fabric opening-angle thermometer (Kruhl, 1998) for sample MR-03, which indicates that deformation had occurred up to 750 °C (with quartz c-axis opening-angle of ca. 95°), compatible with late-magmatic conditions. This suggests that quartz and ferromagnesian minerals were not in isotopic equilibrium, a fact reinforced by the texture-inferred crystallization sequences, which indicate that both amphibole and aegirine precipitated later than quartz.

In spite of the limited number of samples investigated here, $\delta^{18}O$ values recorded in quartz increase somewhat progressively from the undeformed to the highly deformed samples (Fig. 13A). The contrasting value observed for riebeckite may be associated with its post-magmatic crystallization, and the O isotope composition for aegirine from sample MR-47B reflects some kind of post-magmatic overprint; this is supported by its association with post-magmatic riebeckite and magnetite. A similar trend of increasing O isotope values may be inferred for the mafic minerals from the remaining samples; the trend increases smoothly for samples from the massive to the less deformed, coarse-grained granite from the foliated facies (MR-21), and then exhibits an abrupt increase for the most deformed/recrystallized ('protomylonitic') fine-grained sample MR-03 from the foliated facies (Fig. 13A). These results strongly suggest a positive correlation between O isotopic compositions for quartz and the degree of deformation and/or recrystallization, a feature which has been noted by several previous studies including King et al. (1997) in quartz phenocrysts from rhyolites. Hence, the abrupt increase in $\delta^{18}O$ values for amphiboles and aegirine from the lesser- to highly-deformed foliated facies is in agreement with this interpretation.

Using the mineral-water fractionation coefficients of Zheng (1993a, 1993b), the oxygen isotope composition for a potential circulating fluid in samples MR-21 and MR-03 was estimated at a temperature interval between 400 °C to 750 °C, compatible with post- to late-magmatic crystallization stages. The results define a broad yet similar variation in $\delta^{18}O$ values from 2.2 to 7.9‰ in MR-21 (4.7–7.8‰ for quartz, 4.0–5.1‰ for arfvedsonite, and 2.2–3.8‰ for aegirine), and from 3.7 to 8.8‰ in MR-03 (5.6–8.8‰ for quartz, 4.6–7.1% for arfvedsonite, and 3.7–7.2‰ for aegirine), that are in general compatible with the above interpretations.

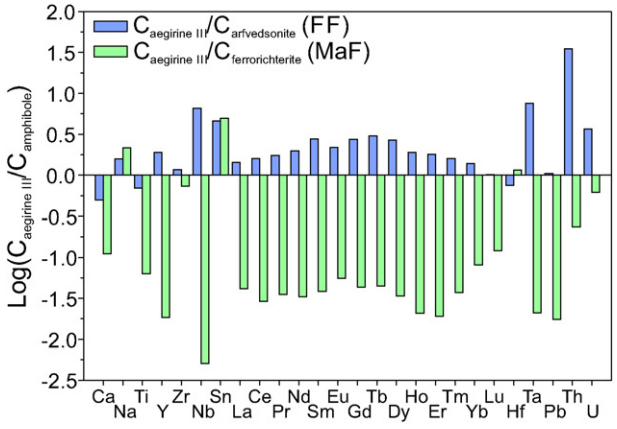

Fig. 12. "Gain–loss" diagram between aegirine III and mantled arfvedsonite and ferrorichterite from the same sample of the foliated (FF) and massive (MaF) facies, respectively.

The influence of the whole-rock compositions on mineral $\delta^{18}O$ values was examined based on the host-rock Agpaitic Index (AI) as shown in Fig. 13B. This diagram depicts well defined correlations between AI and $\delta^{18}O$ values for arfvedsonite and aegirine, and a poor one for quartz; of note, the highly deformed sample MR-03 has a much higher AI than the remaining samples and thus exerts a strong control of the regression lines in Fig. 13. Compared to amphiboles and aegirine from the deformed and microgranitic facies, those from the less-deformed sample MR-21 from the foliated facies record relatively low values for both AI and $\delta^{18}O$, a feature not observed for quartz. These observations suggest some control of the system peralkalinity on the O isotopic signature of the mafic minerals, a feature that is not so evident for quartz. Naturally, in such agpaitic-like systems high AI values are associated with relatively evolved rocks crystallizing at lower temperatures; but in this study this occurs within late- to post-magmatic conditions as supported by microstructural studies. In this regard, integrating all of the textural, geochemical, and isotopic evidences, it is proposed that the deformational events affecting the Papanduva Pluton played an important role in the circulation and concentration of alkali-, F-, HFSE- and REE-rich residual melts and fluids. The combination of deformation/recrystallization and re-equilibration between circulating residual melts/fluids with precipitating phases resulted in the increase of the $\delta^{18}O$ values for quartz. This was accompanied by the late precipitation of relatively ^{18}O-rich arfvedsonite and aegirine, and joined by the crystallization of significant amounts of rare HFSE- and REE-bearing accessory minerals found mostly within the foliated facies.

Increasing system peralkalinity was accompanied by higher oxidizing conditions (e.g., Fig. 4C and D), which leads to the conclusion that deformation events and related chemical redistribution may have also influenced the redox conditions during late crystallization stages, at least in the foliated facies. In such a context, the post-magmatic crystallization of aegirine–augite in this facies took place in a relatively reducing, chemically and probably isotopic distinct environment. In contrast, the common occurrence of miarolitic cavities and pegmatitic dikes in the main massive facies suggest that degassing may have played a role in increasing oxidizing conditions (e.g. Mitchell, 1990).

9. Summary and concluding remarks

Sodic–calcic and sodic amphibole and clinopyroxene are the main ferromagnesian minerals in the massive, deformed, and foliated peralkaline granites and microgranites from the Papanduva Pluton, Morro Redondo Complex. Both amphibole and clinopyroxene precipitated after quartz and alkali feldspar, typical of an agpaitic-like crystallization sequence. Sodic amphiboles are predominant and include arfvedsonite, as well as riebeckite as a typical post-magmatic, hydrothermal phase. Sodic–calcic amphibole corresponds to ferrorichterite and occurs only in the main massive petrographic facies. Clinopyroxene is present as three different textural generations of aegirine, along with occasional aegirine–augite. Aegirine crystallized during late- to post-magmatic stages, subsequent to amphibole crystallization, whereas aegirine–augite is a post-magmatic phase.

Both amphibole and clinopyroxene record evolution trends (from core to crystal rims) towards higher peralkalinity and oxidizing conditions in which the composition of the coexisting melts or fluid phases, along with crystal chemistry controls the HFSE and REE concentrations in these minerals.

$\delta^{18}O$ values in amphibole, clinopyroxene, and quartz crystals from different petrographic facies increase as the degree of sub-magmatic, melt-present deformation increases, affecting portions of the Papanduva Pluton. Within the foliated facies, such deformation exerted influence over the HFSE and REE budgets, as well as the circulation of

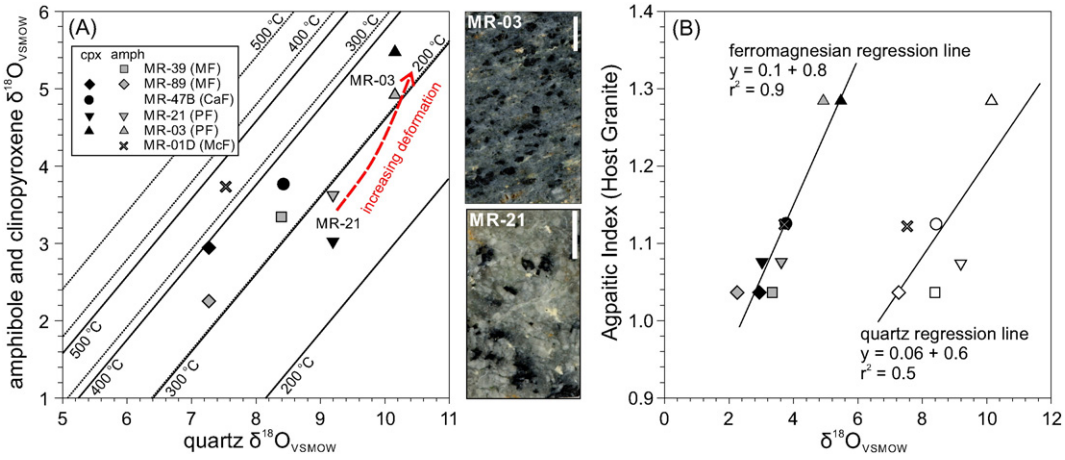

Fig. 13. $\delta^{18}O$ binary diagrams. (A) $\delta^{18}O$ values (‰) of amphibole and clinopyroxene separates against $\delta^{18}O$ values of quartz; isotherms for amphibole (solid lines) and clinopyroxene (dotted lines) calculated after Zheng (1993a, 1993b). (B) $\delta^{18}O$ values (‰) of amphibole, clinopyroxene (black and gray symbols) and quartz separates (white symbols) against the agpaitic indexes of the host-granites. Textural aspects of samples MR-21 (less deformed) and MR-03 (highly deformed/recrystallized) of the foliated facies are also presented in (A). Textures are defined by deformed megacrysts of amphibole (black) and alkali feldspar (white in MR-21) in a saccharoidal quartzo-feldspathic matrix. Vertical white bars equal to 1.0 cm.

residual melts and fluids phases from which amphiboles, clinopyroxenes, and HFSE- and REE-bearing accessory minerals precipitated.

9.1. Intensive crystallization parameters

The textural and chemical findings reported here combined with literature experimental data, permit determination of possible evolution paths in T-fO_2 space for the late melts and fluids associated with the magmatic history of the Papanduva Pluton. Two distinct paths, one grouping the petrographic facies massive, (slightly) deformed, and microgranitic, the other specific for the highly deformed foliated facies, are suggested in Fig. 14 and briefly explained below.

Ferrorichterite is a stable phase under relatively reducing conditions, close to the WM (wüstite-magnetite) buffer at T = 700 °C–750 °C and

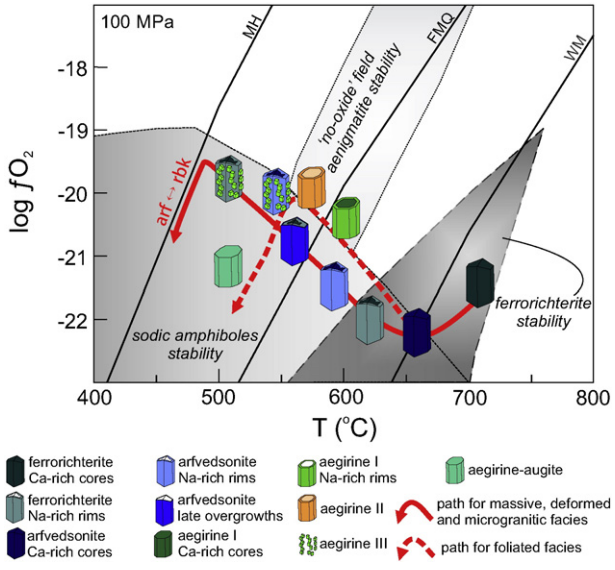

Fig. 14. Inferred evolution paths for magmatic melts and post-magmatic fluids of the Papanduva Pluton in the T-fO_2 space at P_{conf} = 100 MPa showing the crystallization sequence of all amphibole and clinopyroxene textural generations. Sodic amphibole stability field from Ernst (1962); ferrorichterite stability field from Charles (1975); aenigmatite stability field from Nicholls and Carmichael (1969). MH = magnetite–hematite; FMQ = fayalite–magnetite–quartz; and WM = wüstite–magnetite buffers.

P_{fluid} = 100 MPa (Charles, 1975). Its coexistence with arfvedsonite implies an increase of fO_2 to values between the WM and FMQ (fayalite–magnetite–quartz) buffers at T < 700 °C (Ernst, 1962; Stolz, 1986). However, the significant Li contents and the relatively high Fe^{3+}/Fe^{2+} ratios found in many of the investigated arfvedsonite crystals suggest the presence of higher oxidizing conditions, above the FMQ buffer (cf. Marks et al., 2003; Pe-Piper, 2007). According to Bailey (1969), the late crystallization of aegirine in the presence of water indicates relatively higher fO_2, between the FMQ and MH (magnetite-hematite) buffers. The crystallization of aegirine III (Eqs. (5) and (6)) at the expense of the precursor amphiboles is certainly related to late, alkali-rich oxidizing fluids.

In contrast, the assemblage arfvedsonite + aegirine + aenigmatite in the absence of Fe–Ti oxides within the foliated facies places crystallization conditions inside the 'no-oxide' field as defined by Nicholls and Carmichael (1969).

The fO_2 increase during the late- to post-magmatic stages at values close to the MH buffer allowed arfvedsonite replacement by riebeckite which occurred together with magnetite crystallization, in particular within the deformed and microgranitic facies. With progressive crystallization of aegirine in such oxidizing conditions, the Fe^{2+}/Fe^{3+} ratio of the remaining melt/fluid will increase steadily (Markl et al., 2010). This will lead to relatively reduced conditions at the very late stages (cf. Fig. 14) where the activity of alkalis (mainly Na) is also expected to be lower, ultimately promoting the post-magmatic formation of aegirine–augite.

Acknowledgments

We thank the Brazilian Agencies FAPESP (Proc. 08/00562-0) and CNPq (Proc. 305.370/2011-1) for financial support. F. Vilalva benefited from a Doctoral scholarship from CNPq (Proc. 142838/2007-1) and from a Visiting Student scholarship at the University of Notre Dame from CAPES Foundation (Proc. BEX 4956/10-9) during the preparation of this manuscript. The authors are grateful for the constructive comments by Georgia Pe-Piper and Chris Harris, and careful editorial handling and suggestions by Klaus Mezger, which have resulted in an improved manuscript.

Appendix A. Supplementary data

Supplementary data to this article can be found online at http://dx.doi.org/10.1016/j.chemgeo.2015.11.019.

References

Bailey, D.K., 1969. The stability of acmite in the presence of H_2O. Am. J. Sci. 267-A, 1–16.
Blenkinsop, T., 2000. Deformation Microstructures and Mechanisms in Minerals and Rocks. Kluwer Academic Publishers, Dordrecht.
Blundy, J., Wood, B., 1994. Prediction of crystal-melt partition coefficients from elastic moduli. Nature 372, 452–454.
Bonin, B., 2007. A-type granites and related rocks: evolution of a concept, problems and prospects. Lithos 97, 1–29.
Bottazzi, P., Tiepolo, M., Vannucci, R., Zanetti, A., Brum, R., Foley, S.F., Oberti, R., 1999. Distinct site preferences for heavy and light REE in amphibole and the prediction of $^{Amph/L}DREE$. Contrib. Mineral. Petrol. 137, 36–45.
Brown, P.E., Tocher, F.E., 1982. Amphiboles in the lilloise intrusion, east Greenland. Mineral. Mag. 45, 47–54.
Charles, R.W., 1975. The phase equilibria of richterite and ferrorichterite. Am. Mineral. 60, 367–374.
Czamanske, G.K., Dillet, B., 1988. Alkali amphibole, tetrasilicic mica, and sodic pyroxene in peralkaline siliceous rocks, Questa Caldera, New Mexico. Am. J. Sci. 288A, 358–392.
Deer, W.A., Howie, R.A., Zussman, J., 2013. An Introduction to the Rock-forming Minerals. 3rd ed. The Mineralogical Society, London.
Duggan, M.B., 1988. Zirconium-rich sodic pyroxenes in felsic volcanics from the Warrumbungle Volcano, Central New South Wales, Australia. Mineral. Mag. 52, 491–496.
Dyulgerov, M.M., Platevoet, B., 2006. Unusual Ti and Zr aegirine–augite and potassic magnesio-arfvedsonite in the peralkaline potassic oversaturated Buhovo–Seslavtzi Complex, Bulgaria. Eur. J. Mineral. 18, 127–138.
Ernst, W.G., 1962. Synthesis, stability relations and occurrence of riebeckite–arfvedsonite solid solutions. J. Geol. 70, 689–736.
Ferguson, A.K., 1978. The crystallization of pyroxenes and amphiboles in some alkaline rocks and the presence of a pyroxene compositional gap. Contrib. Mineral. Petrol. 67, 11–15.
Frost, C.D., Frost, B.R., 2011. On ferroan (A-type) granites: their compositional variability and modes of origin. J. Petrol. 52, 39–53.
Giret, A., Bonin, B., Leger, J.-M., 1980. Amphibole compositional trends in oversaturated and undersaturated alkaline plutonic ring complexes. Can. Mineral. 18, 481–495.
Grapes, R., Yagi, K., Okumura, K., 1979. Aenigmatite, sodic pyroxene, arfvedsonite and associated minerals in syenites from Morotu, Sakhalin. Contrib. Mineral. Petrol. 69, 97–103.
Gualda, G.A.R., Vlach, S.R.F., 2007a. The Serra da Graciosa A-type granites and syenites, southern Brazil. Part 1: regional setting and geological characterization. An. Acad. Bras. Cienc. 79, 405–430.
Gualda, G.A.R., Vlach, S.R.F., 2007b. The Serra da Graciosa A-Type granites and syenites, southern Brazil. Part 3: magmatic evolution and post-magmatic breakdown of amphiboles of the alkaline association. Lithos 93, 328–339.
Gwinn, R., Hess, P., 1989. Iron and titanium solution properties in peraluminous and peralkaline rhyolitic liquids. Contrib. Mineral. Petrol. 101, 326–338.
Hawthorne, F.C., Ungaretti, L., Oberti, R., Bottazzi, P., Czmanske, G., 1993. Li: an important component in igneous alkali amphiboles. Am. Mineral. 78, 733–745.
Hawthorne, F.C., Ungaretti, L., Oberti, R., Cannillo, E., 1994. The mechanisms of $^{[6]}$Li incorporation in amphiboles. Am. Mineral. 79, 443–451.
Keppler, H., 1993. Influence of fluorine on the enrichment of high field strength trace elements in granitic rocks. Contrib. Mineral. Petrol. 111, 113–121.
King, M.K., Barrie, C.T., Valley, J.W., 1997. Hydrothermal alteration of oxygen isotope ratios in quartz phenocrysts, Kidd Creek mine, Ontario: magmatic values are preserved in zircon. Geology 25, 1079–1082.
Kruhl, J.H., 1998. Reply: prism- and basal-plane parallel subgrain boundaries in quartz: a microstructural geothermobarometer. J. Metamorph. Geol. 16, 142–146.
Mahood, G., Hildreth, W., 1983. Large partition coefficients for trace elements in high-silica rhyolithes. Geochim. Cosmochim. Acta 47, 11–30.
Markl, G., Marks, M.A.W., Frost, B.R., 2010. On the controls of oxygen fugacity in the generation and crystallization of peralkaline melts. J. Petrol. 51, 1831–1847.
Marks, M., Vennemann, T., Siebel, W., Markl, G., 2003. Quantification of magmatic and hydrothermal processes in a peralkaline syenite–alkali granite complex based on textures, phase equilibria, and stable and radiogenic isotopes. J. Petrol. 44, 1247–1280.
Marks, M., Halama, R., Wenzel, T., Markl, G., 2004. Trace element variations in clinopyroxene and amphibole from alkaline to peralkaline syenites and granites: implications for mineral-melt trace-element partitioning. Chem. Geol. 211, 185–215.
Marks, M.A.W., Hettmann, K., Schilling, J., Frost, B.R., Markl, G., 2011. The mineralogical diversity of alkaline igneous rocks: critical factors for the transition from miaskitic to agpaitic phase assemblages. J. Petrol. 52, 439–455.
McDonough, W.F., Sun, S.-S., 1995. The composition of the Earth. Chem. Geol. 120, 223–253.
Mitchell, R.H., 1990. A review of the compositional variation of amphiboles in alkaline plutonic complexes. Lithos 26, 135–156.
Morimoto, N.J., et al., 1988. Nomenclature of pyroxenes. Am. Mineral. 73, 9–10.
Neumann, E.-R., 1976. Compositional relations among pyroxenes, amphiboles and other mafic phases in the Oslo Region plutonic rocks. Lithos 9, 85–109.
Nicholls, J., Carmichael, I.S.E., 1969. Peralkaline acid liquids: a petrological study. Contrib. Mineral. Petrol. 20, 268–294.
Nielsen, T.F.D., 1979. The occurrence and formation of Ti-aegirines in peralkalines syenites. An example from the tertiary ultramafic alkaline Gardner Complex, East Greenland. Contrib. Mineral. Petrol. 69, 235–244.
Njonfang, E., Moreau, C., 2000. The mafic mineralogy of the Pandé massif, Tikar plain, Cameroon, implications for a peralkaline affinity and emplacement from highly evolved alkaline magma. Mineral. Mag. 64, 525–537.
Njonfang, E., Nono, A., 2003. Clinopyroxene from some felsic alkaline rocks of the Cameroon Line, central África: petrological implications. Eur. J. Mineral. 15, 527–542.
O'Halloran, D.A., 1985. Ras ed Dom migrating ring complex: A-type granites and syenites from the Bayuda Desert, Sudan. J. Afr. Earth Sci. 3, 61–75.
Olin, P.H., Wolff, J.A., 2010. Rare earth and high field strength element partitioning between iron-rich clinopyroxenes and felsic liquids. Contrib. Mineral. Petrol. 160, 761–775.
Papoutsa, A., Pe-Piper, G., 2014. Geochemical variation of amphiboles in A-type granites as an indicator of complex magmatic systems: Wentworth pluton, Nova Scotia, Canada. Chem. Geol. 384, 120–134.
Pe-Piper, G., 2007. Relationship of amphibole composition to host-rock geochemistry: the A-type gabbro–granite Wentworth pluton, Cobequid shear zone, eastern Canada. Eur. J. Mineral. 19, 29–38.
Piilonen, P., McDonald, A.M., Poirier, G., Rowe, R., Larsen, A.O., 2013. Mafic minerals of the alkaline pegmatites in the Larvik plutonic complex, Oslo Rift, Southern Norway. Can. Mineral. 51, 735–770.
Prowatke, S., Klemme, S., 2005. Effect of melt composition on the partitioning of trace elements between titanite and silicate melt. Geochim. Cosmochim. Acta 69, 695–709.
Reguir, E., Chakhmouradian, A.R., Pisiak, L., Halden, N.M., Yang, P., Xu, C., Kynický, J., Couëslan, C.G., 2012. Trace-element composition and zoning in clinopyroxene- and amphibole-group minerals: implications for element partitioning and evolution of carbonatites. Lithos 128-131, 27–45.
Roelofsen, J.N, Martin, R.F., 1997. The mafic silicates of the Strange Lake peralkaline complex, Quebec-Labrador. I. Primary arfvedsonitic amphibole and aegirine, in: Roelofsen, J.N., The primary and secondary mafic silicates of two alkaline anorogenic complexes: Strange Lake (Quebec-Labrador) and Amba Dongar (Gujarat, India). Unpublished PhD Thesis. Department of Earth and Planetary Sciences, McGill University, Montreal, pp. 144–205.
Salvi, S., Williams-Jones, A.E., 1990. The role of hydrothermal processes in the granite-hosted Zr, Y, REE deposit at Strange Lake, Quebec/Labrador: evidence from fluid inclusions. Geochim. Cosmochim. Acta 54, 2403–2418.
Salviulo, G., Secco, L., Marzoli, A., Piccirillo, E.M., Nyob'e, J.B., 2000. Ca-rich pyroxene from basic to silicic volcanic rocks from the Cameroon Volcanic Line (West-Africa): crystal chemistry and petrological relationships. Mineral. Petrol. 70, 73–88.
Scaillet, B., Macdonald, R., 2001. Phase relations of peralkaline silicic magmas and petrogenetic implications. J. Petrol. 42, 825–845.
Schilling, J., Marks, M.A.W., Wenzel, T., Vennemann, T., Horváth, L., Tarassoff, P., Jacob, D.E., Markl, G., 2011. The magmatic to hydrothermal evolution of the intrusive Mont Saint-Hilaire Complex: insights into the late-stage evolution of peralkaline rocks. J. Petrol. 52, 2147–2185.
Shearer, C.K., Papike, J.J., Karner, J.M., 2006. Pyroxene europium valence oxybarometer: effects of pyroxene composition, melt composition, and crystallization kinetics. Am. Mineral. 91, 1565–1573.
Shellnutt, J.G., Iizuka, 2011. Mineralogy from three peralkaline granitic plutons of the Late Permian Emeishan large igneous province (SW China): evidence for contrasting magmatic conditions of A-type granitoids. Eur. J. Mineral. 23, 45–61.
Stolz, A.J., 1986. Mineralogy of the Nandewar volcano, northeastern New South Wales, Australia. Mineral. Mag. 50, 241–255.
Strong, D.F., Taylor, R.P., 1984. Magmatic-subsolidus and oxidation trends in composition of amphiboles from silica-saturated peralkaline igneous rocks. Tschermaks Mineral. Petrogr. Mitt. 32, 211–222.
Tiepolo, M., Oberti, R., Zanetti, A., 2007. Trace-element partitioning between amphibole and silicate melt. Rev. Mineral. Geochem. 67, 417–452.
Vilalva, F.C.J., Vlach, S.R.F., 2014. Geology, petrography and geochemistry of the A-type granites from the Morro Redondo Complex (PR-SC), South Brazil, Graciosa Province. An. Acad. Bras. Cienc. 86, 85–116.
Vilalva, F.C.J., Vlach, S.R.F., Simonetti, A., 2013. Nacarebiosite-(Ce) and britholite-(Ce) in peralkaline granites from the Morro Redondo Complex, Graciosa Province, Southern Brazil: occurrence and compositional data. Can. Mineral. 51, 313–332.
Vlach, S.R.F., Siga Jr., O., Harara, O.M.M., Gualda, G.A.R., Basei, M.A.S., Vilalva, F.C.J., 2011. Crystallization ages of the A-type magmatism of the Graciosa Province (Southern Brazil): constraints from the zircon U-Pb (ID-TIMS) dating of coeval K-rich gabbro-dioritic rocks. J. S. Am. Earth Sci. 32, 407–415.
Wood, B.J., Blundy, J.D., 1997. A predictive model for rare earth element partitioning between clinopyroxene and anhydrous silicate melt. Contrib. Mineral. Petrol. 129, 166–181.
Zack, T., Foley, S.F., Jenner, G.A., 1997. A consistent partition coefficient set for clinopyroxene, amphibole and garnet from laser ablation microprobe analysis of garnet pyroxenites from Kakanui, New Zealand. N. Jb. Mineral. (Abh.) 172, 23–41.
Zheng, Y.-F., 1993a. Calculation of oxygen isotope fractionation in anhydrous silicate minerals. Geochim. Cosmochim. Acta 57, 1079–1091.
Zheng, Y.-F., 1993b. Calculation of oxygen isotope fractionation in hydroxyl-bearing silicates. Earth Planet. Sci. Lett. 120, 247–263.